1	Novel NiAl-strengthened high entropy alloys with balanced tensile strength and	
2		ductility
3	Haoyan Diao ^a , Dong Ma ^b , Rui Feng ^a , Tingkun Liu ^a , Chao Pu ^a , Chuan Zhang ^c , Wei Guo ^d ,	
4		Jonathan D. Poplawsky ^d , Yanfei Gao ^{a,*} , Peter K. Liaw ^{a,*}
5	a.	Department of Materials Science and Engineering, University of Tennessee,
6		Knoxville, TN 37996, USA
7	b.	Neutron Scattering Division, Neutron Sciences Directorate, Oak Ridge National
8		Laboratory, Oak Ridge, TN 37831, USA
9	c.	CompuTherm LLC, Middleton, WI 53562, USA
10	d.	Center for Nanophases Materials Sciences, Oak Ridge National Laboratory, 1
11		Bethel Valle Rd., Oak Ridge, TN 37831, USA
12		
13		
14		
15		
16	* Corresponding authors: <u>ygao7@utk.edu</u> ; <u>pliaw@utk.edu</u>	
17		

Abstract:

- A single phase, face-centered-cubic (FCC) Al_{0.3}CoCrFeNi high entropy alloy usually has low yield strength. Here, a precipitate-strengthened Al_{0.3}CoCrFeNi has been developed, exhibiting enhanced yield strength while retaining good ductility, which is attributed to a novel microstructure comprising a finely distributed, needle-like B2 phase within the grains of the FCC matrix and a granular σ phase along the grain boundaries. Such a microstructure was obtained by a two-step heat treatment of an as-cast Al_{0.3}CoCrFeNi, whose parameters were determined by integrating CALPHAD-based thermodynamic calculations with microstructural characterization by atom probe tomography. *In situ* neutron diffraction, in conjunction with crystal-plasticity finite-element simulations, has revealed the strengthening effect owing to the load partitioning between the constituent phases. This work has important implications for understanding phase stability and deformation mechanisms in multi-principal component alloys, and paves the way for developing novel microstructures in complex alloys using correlative techniques.
- **Key Words**: High entropy alloys; tensile strength; atom probe tomography; in situ neutron diffraction; thermodynamic calculations

1. Introduction

Most structural materials for engineering applications are based on single principal elements, e.g., Al-, Ti-, Fe-, and Ni-based superalloys. The creation and design of novel structural materials with enhanced mechanical properties have always been the goal of many scientists and engineers. Recently, high entropy alloys (HEAs) [1-5], also known as multicomponent alloys [1], multi-principal element alloys (MPEAs) [6], complex concentrated alloys (CCAs) [5], compositionally complex alloys (CCAs) [4], baseless alloys (BAs) [5], or metal buffets (MBs) [7] have revolutionized alloy design approaches by employing the use of five or more multi-principal elements in an equal or near-equal atomic percent, which offer a vast alloy compositional space with potential outstanding properties [1-3].

While the reported literatures on HEAs indicate promising enhancements in mechanical properties, such as higher hardness [1], better yield strengths [8-12], comparable or greater fatigue resistance [13-16], and superior fracture toughness [17], relative to conventional alloys, strategic processing is still needed to make HEAs into real engineering alloys for industrial applications [7]. One of the approaches is the grain refinement. For example, Otto et al. increased the room temperature (RT) yield strength of CoCrFeMnNi from 200 MPa to 350 MPa via the grain refinement from 155 to 4.4 μm, utilizing the grain-boundary strengthening mechanism [9]. Similarly, Gangireddy et al. [18] and Gwalani et al. [19] also employed the grain-boundary strengthening strategy to the Al_{0.3}CoCrFeNi alloy, finding remarkable Hall-Petch strengthening with a Hall-Petch constant of 811 and 824 MPa/μm^{0.5}, respectively. Another approach is precipitation strengthening via heat treatment processing. Recently, the strength increase due to the

second phase precipitation has been reported through the thermo-mechanical processing [20, 21]. Due to the formation of the σ phase, significant strengthening (from 130 MPa to 330 MPa), accompanied by no ductility, was demonstrated in the CoCrFeNiV alloys [20]. Minor alloy additions of Ti and Al to a single-phase CoCrFeNi HEA can induce the formation of L1₂-coherent precipitates in the FCC matrix, which gives a yield strength of 645 MPa with an elongation of 39 % [21]. Furthermore, through controlling the transformation pathways of Al_{0.3}CoCrFeNi HEA, both grain-boundary strengthening and precipitation strengthening were utilized to improve the tensile properties of Al_{0.3}CoCrFeNi HEA, resulting in a great enhancement of strength from 230 MPa to 820 MPa without too much ductility reduction [22]. Actually, after the grain refinement and the introduction of precipitates, not only the tensile properties of Al_{0.3}CoCrFeNi can be optimized, but also the fatigue resistance can be greatly enhanced [23]. Although the precipitation strengthening has been utilized to improve strengths of the soft single phase HEAs, more detailed investigations are required to understand the strengthening effect of precipitates, and micromechanical deformation behavior between the precipitates and the matrix. In order to solve this critical issue, the present work focuses on the strategically developing second-phase-strengthened HEAs with the balanced tensile strength and ductility by coupling experimental and computational efforts.

57

58

59

60

61

62

63

64

65

66

67

68

69

70

71

72

73

74

75

76

77

78

79

The three dimensional (3D) atom probe tomography (APT) [24] has been used to visualize the nano-scaled distribution of alloying elements in Al_{0.5}CoCrCuFeNi [25], AlCoCrCuFeNi [26-28], Al_{1.3}CoCrCuFeNi [29], AlCrCuFeNiZn [30], AlCoCrFeNi [31], and CoCrFeMnNi [32-34] HEAs, and the nature of interfaces between constituent phases in the AlCoCrCuFeNi HEA [24, 26, 27]. The chemical distribution phenomenon on the

atomic level has been seldom studied in the Al_{0.3}CoCrFeNi HEAs. In situ neutron diffraction (ND) techniques subjected to continuous tensile loading provides deformation behaviors and mechanisms as a function of temperature in single-phase CoCrFeMnNi [35, 36]. However, the systematical study of the micro-mechanical deformation behavior of multi-phase HEAs is still limited [7].

In the current work, we present stable phases and their fractions, as well as the distribution of each alloying element within different phases, of Al_{0.3}CoCrFeNi within the temperature range from 200 to 1,500 °C, using the calculation of phase diagrams (CALPHAD) approach [37-43]. Then based on the thermodynamic calculation results, a two-step heat treatment processing (homogenized at 1,250 °C and then aged at 700 °C) was designed to achieve optimal microstructure combinations with good mechanical properties. The micromechanical deformation behavior of the B2, i.e., ordered body-centered-cubic (BCC) structure, in the FCC matrix is studied using the in situ neutron diffraction measurements [44]. The grain-level information, e.g., how the applied load is partitioned among different grain families in the single-phase HEAs and between two phases in the dual-phase HEAs, are derived from neutron results. The crystal-plasticity finite-element simulation (CPFEM) was utilized to simulate the elastic-plastic response of (hkl) lattice strains [44] as a function of stress at RT and to compare the prediction with the neutron experimental results quantitatively.

The coupled experimental and computational efforts can optimize engineering properties and significantly facilitate the application of HEAs as future high temperature materials. At the same time, the study could deepen our fundamental understanding of the

phase stability and strengthening mechanisms of both single-phase and multi-phase HEAs through the integration of experimental and theoretical approaches.

2. Methods

2.1. Sample preparation

The Al_{0.3}CoCrFeNi with a nominal chemical composition of 7.00Al-23.26Co-23.26Cr-23.26Fe-23.26Ni (atomic percentage (at. %)) was fabricated by vacuum-induction melting to a plate (~ 127 mm × 305 mm × 19 mm). Then the specimen has undergone the hot-isostatic-pressing (HIP) process at 1,204 °C and 103 MPa for 4 hours. After that, Al_{0.3}CoCrFeNi was quartz-tubed with the triple-pumped argon and underwent two different heat treatments. One is the homogenization treatment at 1,250 °C for 2 hours (h), followed by water quenching (as-homogenized). Another is aging at 700 °C for 500 h after the 1,250 °C homogenization and then, water quenched (as-aged). Note that the annealing parameters were selected based on the CALPHAD predictions, as described in more details in Section 3.1.

2.2. Microstructural characterization

Atom probe tomography (APT) was performed at the Oak Ridge National Laboratory (ORNL) Center for Nanophase Materials Sciences (CNMS) [45]. The region of interest was extracted as a wedge, and mounted to a Si-post array, using an FEI Nova 200 focused ion beam (FIB) system and micromanipulators. Then the specimen is further sharpened into a needle, with a diameter of less than 100 nm by a series of annular milling patterns. The APT experiments were conducted with a local electrode atom probe (CAMECA Instruments LEAP 4000X HR) at the base temperature of ~ 50 K (- 223 °C).

- At least 5 million ions were collected for each sample to ensure adequate data statistics.
- The datasets were reconstructed and analyzed using the IVAS 3.6.8 software [45].
 - The 700 °C aged state was characterized by the scanning electron microscopy (SEM), using the FEI Nova instrument. The SEM specimen was prepared by a vibration polishing method after a finer grinding with a 1,200 grit SiC paper. The size (i.e., width and length) and volume fraction of needle-like B2 precipitates distributed in the FCC matrix was measured, using the software package Image-Pro Plus (version 6.0; Media Cybernetics, Baltimore, MD). Total 300 needles were counted for the size analysis and all the needle-like region observed in the SEM image was used for the volume fraction analysis.

2.3. Mechanical Testing

- Before the in situ neutron tensile testing, tensile tests experiments conducted in advance on the as-homogenized and as-aged HEAs at RT with a strain rate of $5 \times 10^{-5} \, \text{s}^{-1}$, using an MTS Model 810 servohydraulic machine. The dimensions of the cylindrical dog-bone specimen for the laboratory tensile test were 28 mm in gage length and 3.175 mm in diameter.
- *2.4.* In situ tensile tests performed in the neutron diffraction facility
 - In situ neutron diffraction (ND) experiments were performed at the VULCAN Engineering Materials Diffractometer of the Spallation Neutron Source (SNS), Oak Ridge National Laboratory (ORNL). VULCAN [46, 47] is a time-of-flight (TOF) neutron diffractometer using neutron pulses with a range of wavelengths (~ 0.5 8 Å), which is optimized to measure elastic strains at precise locations in bulk specimens. The experimental loading rig is mounted with its loading axis oriented horizontally and at 45°

to the incident beam, with two detectors oriented at 90° to this beam (see Fig. 1). The two stationary detector banks collect simultaneously two complete diffraction patterns in the axial and radial directions, respectively. Diffraction from the crystal lattice of grains, whose plane normal (that is, <hkl>) is parallel to the axial or radial directions, will be detected, and the lattice spacing, d_{hkl} , can, thus, be measured from the diffraction peak, corresponding to the (hkl) reflection. The dimensions of the cylindrical dog-bone specimen for the in situ tensile test were 50 mm in length and 6.35 mm in diameter. Figure 1(a) is the schematic of the real time in situ neutron diffraction setup at VULCAN, SNS, ORNL. The incident beam size is 5 mm \times 5 mm. About 700 grains should be able to be included within the 5 mm \times 5 mm beam size. The measuring time for each stress level is \sim 10 min. The strain is determined parallel to the applied load, using an extensometer. Figure 1(b) presents the enlarged gauge volume under neutron diffraction.

2.5. Thermodynamic modeling

The phase diagrams and thermodynamic properties of the Al_{0.3}CoCrFeNi HEAs are predicted by the phenomenological Calculation of Phase Diagrams (CALPHAD) approach, using PanHEA database [37-42]. The CALPHAD approach is based on the thermodynamic law that a system reaches its equilibrium when it attains the lowest Gibbs energy for a given composition, temperature, and pressure. The thermodynamic description for higher-order HEA systems is obtained via the extrapolation from its constituent lower-order systems, such as binary and ternary systems [48]. A thermodynamic database for the Al–Co–Cr–Fe–Ni system was developed in the entire composition region. Details of these thermodynamic models can be found in References [37-42].

Both BCC and FCC phases are described by the substitutional solution model (Al, Co, Cr, Fe, and Ni). The B2 phase is described by the compound energy formalism: (Al,

172 Co, Cr, Fe, and Ni)_{0.5}: (Al, Co, Cr, Fe, and Ni)_{0.5}. The Gibbs energy is expressed as,

173
$$G_m^{B2} = \sum_{i} \sum_{j} y_i^{I} y_i^{II} G_{i:j}^{B2} + RT(0.5 \sum_{i} y_i^{I} \ln y_i^{I} + 0.5 \sum_{i} y_i^{II} \ln y_i^{II}) + G_m^{ex,B2}$$
 (1)

where $y_i^{\rm I}$ and $y_i^{\rm II}$ are the species concentrations of the component, i, in the first and second sublattices, respectively. $G_{i:j}^{B2}$ is the Gibbs energy of the B2 phase. The first term on the right hand of the equation represents the reference state with a mechanical mixture of the stoichiometric compound with a B2 structure: $i_{0.5}j_{0.5}$. The second term is the ideal mixing term with a gas constant, R, and the temperature, T, in Kelvin. The last term is the excess Gibbs energy of mixing, The PANDAT software [37-41, 43] was performed under the PanPhaseDiagram module for the present work.

2.6. Crystal-plasticity finite-element modeling (CPFEM)

A CPFEM is developed to predict the lattice strain evolution during the tensile test in HEA materials. The slip-based crystal-plasticity model considered the slip deformation inside each grain, and the yielding sequence of different grains is governed by the grain orientation, elastic constants, and Schmid factors of specific slip systems. The constitutive parameters include elastic constants, C₁₁, C₁₂, and C₄₄, the critical resolved shear stress, τ₀, and those describing the strain rate dependence and strain hardening behavior. The concise description of the crystal plasticity theory and its constitutive equations can be found in the references [49-51]. Two representative volume element (RVE) models were constructed, respectively, due to the different microstructures of the HEAs studied in the tensile tests. For the Al_{0.3}CoCrFeNi (after homogenization at 1,250 °C for 2 h) preserving a single FCC phase, the RVE was built

by 1,000 cubic grains with each cubic grain containing 4 three dimensional eight node brick elements in the random crystallographic orientation distribution. The RVE model for the Al_{0.3}CoCrFeNi (after aging at 700 °C for 500 h) was created, based on the microstructure observation (as will be shown in Fig. 10(a)) showing the mixture of an FCC matrix and needle-like B2 phase. This model aggregates 1,000 cubic grains, in which a collection of $3 \times 3 \times 3$ cubic units are composed of an FCC matrix grain and a B2 grain. Specifically, the needle-like B2 phase is embedded into the FCC matrix in the middle of the $3 \times 3 \times 3$ cubic unit. Similarly, the grain orientation is random for both FCC and B2 phases. The faces of both RVE models with normal directions of x, y, and z, as will be shown in Fig. 10(a) are prescribed to the symmetric boundary conditions. A ramping displacement with a constant rate is applied on the surface with a z normal direction. The diffraction vector is parallel to the loading direction, which is the z direction. This simulation has been implemented in a commercial finite element software, ABAQUS, through the modified user-defined material (UMAT) subroutine [52] to investigate the lattice strain evolution in a polycrystalline aggregate. The calculated {hkl} lattice strain was a volume average of the projected elastic strains in a subset of grains, whose {hkl} plane normal direction was parallel to the diffraction vector.

3. Results

193

194

195

196

197

198

199

200

201

202

203

204

205

206

207

208

209

210

212

213

214

3.1. CALPHAD analysis and phase stability at both 1,250 °C and 700 °C

Figure 2(a) presents the equilibrium phase diagram of the Al_{0.3}CoCrFeNi HEA, provided by the CALPHAD thermodynamic calculations. One can see that under an equilibrium condition, its melting temperature is about 1,427 °C. Then the liquid was

transformed into the FCC solid phase, which is the only one stable phase in the temperature range from 1,028 to 1,427 °C. Below 1,028 °C, the ordered B2 phase precipitates out from the FCC matrix. As the temperature goes down to 725 °C and 606 °C, σ and L1₂ phases start to form, respectively. According to phase diagram (Fig. 2(a)), the alloy is composed of a pure FCC phase, when the annealing temperature is 1,250 °C. When it is annealed at 700 °C for a sufficient time, the alloy consists of FCC, B2, and σ phases. More detailed information, e.g., chemical compositions of each phase at two annealing temperatures (1,250 °C and 700 °C), from our thermodynamic calculations, is listed in Fig. 2(b), which indicates that the FCC phase is homogenous with the nominal chemical composition of the Al_{0.3}CoCrFeNi, the ordered B2 phase is NiAl rich, and the σ phase is Cr rich. The comparison between thermodynamic calculations with APT experimental results will be discussed in Section 4.3.

3.2. Microstructures of the Al_{0.3}CoCrFeNi after annealing at 1,250 °C for 2 hours

The 3D APT elemental maps of the Al_{0.3}CoCrFeNi HEA after annealing at 1,250 °C for 2 hours in Fig. 4(a) show that the distributions of Al, Co, Cr, Fe, and Ni elements within the analyzed volume, $35 \times 35 \times 75$ nm³, are homogeneous with no indication of segregation or clustering on the atomic scale. Shown in Fig. 4(b), the concentrations of the different elements, Al, Co, Cr, Fe, and Ni, along with the black arrow in Fig. 4(a), represent small concentration fluctuations. In order to quantify the concentration fluctuations, the frequency distribution of nanoscaled atomic clusters obtained from the experimental APT data is compared with the classical binomial frequency distribution, f(n) [53]. The deviation of the experimentally measured distribution from the binomial can be quantified, by means of the normalized χ^2 statistics,

μ [53]. μ can track the changes in the degree of solute segregation. When μ is equal to 0,
 it means a random distribution. But when μ is 1, it suggests a complete association in the
 occurrence of the solute atoms.

241
$$f(n) = \binom{n}{k} p^k (1-p)^{n-k}$$
 (2)

242 where n is the number of solute atoms.

243
$$\chi^2 = \sum_{n=0}^{N} \frac{(e(n) - f(n))^2}{f(n)}$$
 (3)

where e(n) is the number of blocks containing n solute atoms in the experimental data.

$$0 \le \mu = \sqrt{\frac{\chi^2}{N + \chi^2}} \le 1 \tag{4}$$

where N is the number of blocks sampled.

250

251

252

253

254

255

The μ values for Al, Co, Cr, Fe, and Ni were found to be 0.1138, 0.0389, 0.0520, 0.0349, and 0.1042, respectively, which confirm that the Al, Co, Cr, Fe, and Ni distributions are indeed homogenous after annealing at 1,250 °C for 2 hours.

3.3. Precipitate phases and morphologies after the heat treatment at 700 °C for 500 h

In order to increase the yield strength of the $Al_{0.3}CoCrFeNi$ HEA, two-step heat treatments were performed, with the assistance of thermodynamic modeling (Section 3.1). The microstructure after aging at 700 °C for 500 h within a grain is shown in Fig. 4. The SEM image shows that needle-like second phases appear in the matrix (Fig. 4(a)). The average width of the needle-like phases is ~ 162 nm determined by Image-Pro Plus.

Moreover, the determined volume fraction of these second precipitate is ~14%, which is very consistent with the CALPHAD prediction (~12%). APT is used to obtain the chemical distribution and interfacial configuration of the needle-like precipitates on the nanometer level. The atom maps of the constituent elements for the Al_{0.3}CoCrFeNi HEA after aging at 700 °C for 500 h are shown in Fig. 4(b). The dimension of the second phase, ~ 140 nm, is consistent with the SEM results. The concentration profile of all alloying elements within both the second phase and the matrix is shown in Fig. 4(c). The results indicate that the second phase is the Al-Ni-rich phase. Due to the present of BCC based structure revealed by the diffraction patterns (Fig. 8(b) and 8(c)), the Al-Ni rich phase is the B2 phase, despite of the unobserved (001) superlattice peak for B2. The comparison between the APT experimental results and thermodynamic calculations will be discussed in Section 4.5.

The distribution of chemical compositions after aging at 700 °C for 500 h from the grain boundary region is shown in Fig. 5. The atomic maps (Fig. 5(a)) and the proximity histogram across the interface between the FCC matrix and grain boundary precipitates (Fig. 5(b)) indicate the presence of Cr-rich σ precipitates (Figure 5(b)). In the FCC matrix, it has a concentration of 0.276 at.% Al, 40.480 at.% Co, 8.466 at.% Cr, 47.902 at.% Fe, and 2.876 at.% Ni. In the σ phase, it has a concentration of 0.016 at.% Al, 25.112 at.% Co, 54.240 at.% Cr, 18.277 at.% Fe, and 0.236 at.% Ni (Table 3(a)).

275 3.4. Tensile properties of $Al_{0.3}CoCrFeNi$ after homogenization at 1,250 °C for 2 h and 276 aging at 700 °C for 500 h

The full stress-strain curves of both as-homogenized and as-aged HEAs are provided in Figs. 6 (a) and (b). The yield strength and ductility of as-homogenized state are about 167 MPa and 62%, respectively. After the aging at 700 °C for 500 h, the yield strength of this HEA increase to 321 MPa, but the ductility decreases to 29%. The observed tensile yield strength and ductility of the 1,250 °C-homogenized HEA are very similar to the previously reported values [19, 54]. However, the tensile yield strength and ductility of the 700 °C-aged one are very different from those reported results [19, 22]. This is because the very different volume fraction, morphology of B2 precipitates, and the grain size of FCC matrix [19, 22]. One can note that the serrated flow happened in the 1,250 °C-homogenized single-phase FCC HEA, but not 700 °C-aged B2 precipitated strengthened HEA, which is related to the localized heterogeneous deformation [55, 56]. It should be also noted that the serrated flow in the 1,250 °C-homogenized single-phase FCC HEA is not observed during the in situ neutron tensile testing, which is due to the limited data acquisition frequency during in situ testing. One will notice that the laboratory measured yield strengths of both states will be slightly higher than those measured during the in situ neutron tensile tests (~ 20 MPa). The small difference can be ascribed to the different mechanical testing machine, testing strain rate, and sample size. In order to utilize the information captured by in situ neutron diffraction and explain the effect of B2 strengthening, all the yield strengths that we used will from the results during the in situ neutron tensile testing.

277

278

279

280

281

282

283

284

285

286

287

288

289

290

291

292

293

294

295

296

297 3.5. In situ Characterization of Lattice Strain Evolution during Tension of 298 Al_{0.3}CoCrFeNi after Homogenization at 1,250 °C for 2 h In situ neutron diffraction techniques [35, 36] subjected to continuous tension are used to study lattice strain changes as a function of stress in Al_{0.3}CoCrFeNi after homogenization at 1,250 °C for 2 h. The macroscopic stress-strain behavior during in situ tension at RT was measured (Fig. 7(a)). In the elastic region, the machine is under a stress-control mode, i.e., the tension tests are interrupted and hold for 10 minutes at 20, 40, 60, 80, 100, 120, and 140 MPa, respectively. Then the machine is under a strain-control mode. The macroscopic stress-strain curve is shown in Fig. 8(a). The yield strength is around 145 MPa.

The neutron scattering geometry allows for simultaneous measurements of two scattering vectors, which are parallel and perpendicular to the tensile axis, respectively. Diffraction from the crystal lattice of grains, whose plane normal (that is, <hkl>) is parallel to the loading direction and satisfies Bragg's law, is detected by Bank 1. At the same time, the diffraction pattern from the crystal lattice, whose plane normal is perpendicular to the loading direction and satisfies Bragg's law, is detected by Bank 2 (Fig. 1). Figures 7(b) and 7(c) show the typical diffraction patterns of the Al_{0.3}CoCrFeNi HEA after homogenization at 1,250 °C for 2 h from Banks 1 and 2, respectively, measured at RT, with a 10-minute data collection. All peaks are indexed to an FCC structure, presented in Figs. 7(b) and 7(c). The intensity difference between Figs. 7(b) and 7(c) indicates that the material has a strong texture.

The hkl plane-specific lattice strain is grain orientation dependent and described as the average lattice strain accumulated in the diffracted grains, whose hkl plane normal is parallel to the diffraction vector, Q. In the Al_{0.3}CoCrFeNi HEA, the hkl plane-specific lattice strain is determined by

$$\varepsilon_{hkl} = \left(d_{hkl} - d_{hkl}^{0}\right) / d_{hkl}^{0} \tag{5}$$

where ε_{hkl} is the lattice strain in the hkl-oriented grains, d_{hkl}^0 is the reference lattice spacing before deformation under the unloaded state, and d_{hkl} is the d spacing as a function of the applied stress, for the respective phases.

The lattice strain evolution of <200>, <220>, <311>, and <331> within the Al_{0.3}CoCrFeNi after homogenization at 1,250 °C for 2 h during tensile deformation at room temperature is shown in Fig. 7(d). The results illustrate that the lattice strain change is strongly dependent on grain orientations, indicative of the strong elastic anisotropy. The {200} grains exhibit the largest elastic strain along the loading direction and a significant shift, relative to their linear elastic response, which manifests the elastic-plastic transition. The {311} grains have the second largest elastic strain but maintain nearly a linear response. The {220} and {113} grains, on the other hand, have a lower elastic strain, indicating that they have a larger elastic stiffness.

3.6. In situ Characterization of Lattice strain Evolution during Tension of Al_{0.3}CoCrFeNi after aging at 700 °C for 500 h

In situ ND techniques are also utilized to investigate the deformation behavior of the multiphase Al_{0.3}CoCrFeNi after aging at 700 °C for 500 h. The macroscopic stress-strain behavior during in situ tension at RT is presented in Fig. 8(a), where the 0.2 % proof stress of Al_{0.3}CoCrFeNi (after aging at 700 °C for 500 h) was determined as 300 MPa. Figures 8(b) and 8(c) show typical diffraction patterns of Al_{0.3}CoCrFeNi after aging at 700 °C for 500 h, measured by the Bank 1 and Bank 2 detectors, respectively, at RT

with a 10-minute data collection. Besides FCC peaks, at least three peaks, <110>, <200>, and <211> of a secondary phase, a B2 phase, are present.

The evolution of the specific {hkl} lattice strains of the FCC matrix and B2 phase as a function of average stress at room temperature are displayed in Fig. 8(d). At 300 MPa, the slope of the elastic strain of the FCC matrix is increased, relative to the linear elastic response, while the slope of the elastic strain of the B2 phase is reduced.

3.7. *Crystal-plasticity finite-element modeling*

Details of the hardening law and other constitutive parameters can be found in the Table 1, where C_{11} , C_{12} , and C_{44} are elastic constants, n is the rate sensitivity exponent, h_0 is the initial hardening modulus, τ_s is the saturation slip strength, τ_0 is the initial slip strength, and q is the ratio of latent over self-hardening behavior. The input elastic constants are obtained by fitting the Kröner model [57, 58] and our simulation will further fine tune these values so as to fit the initial lattice strains when all grains and phases are in the elastic deformation. Note that the initial lattice strain splitting is primarily determined by the Schmid factor (which is controlled by the choice of slip systems) and the directional modulus (which is governed by the elastic anisotropy). The slip system is chosen as the {110} <111> system for the B2 phase, and as the {111} <110> for the FCC phase. The initial slip strength, τ_0 , can be estimated from the deviation of the lattice strain from linearity, as the applied stress increases and exceeds the elastic stage. In single phase polycrystalline materials, τ_0 relates to the macroscopic yield stress by the Taylor factor, being about 3.0 for random textured FCC and BCC polycrystalline

materials. This is how we estimate τ_0 for the soft FCC phase. It is assumed that the B2 phase does deform elastically in the overall tensile test.

The predicted results of the macro stress-strain curve and lattice strain evolution are illustrated in the Figs. 9 and 10 for single-phase and dual-phase HEAs, respectively. The scattered spots denote experimental data, and the solid line represents simulation results. From Fig. 9(c), the stress-strain curve can estimate macro-deformation behavior, illustrating that calculated lattice strains accurately predict the experimental results. Lattice strain splitting in the elastic deformation indicates the elastic anisotropy of different {hkl} grain families, which agree with the observed behaviors. After yielding, the stresses transfer among different {hkl} grain families. Some hard-oriented grains undergo higher stresses (thus having larger lattice strains) and soft-oriented grains undertake lower stress (thus having lower lattice strains), which results in lattice strain increases nonlinearly during plastic deformation.

Figure 10(b) shows the stress distribution in the RVE after deformation for Al_{0.3}CoCrFeNi (after aging at 700 °C for 500 h). The highlight green cubic units represent grains of the B2 phase, which indicates that the B2 phase undergoes much higher stress than the FCC phase after plastic deformation. The lattice strain evolution of two-phase HEAs as a function of stress predicted by CPFEM is shown in Fig. 10(c), in comparison to the experimental measurement during in situ tension at RT. The solid lines in Fig. 10(c) are predictions, while the symbols are experimental data. In Fig. 10(c), the predicted results capture the stress partitioning. After yielding, the increase rate of the lattice strain of the B2 phase drops dramatically. However, the lattice strain of the FCC phase still increases linearly. The huge splitting of FCC and B2 phases explain the stress

partitioning in this kind of the dual-phase HEA. As a hard phase, the B2 phase has not yielded during the tensile test. Consequently, the stresses transfer to the B2 phase, which will enable an overall higher degree of plastic deformation. The strengthening B2 phase delays the localized failure by the stress transfer. Some deviation between the predicted and experimental results is likely due to the microstructure simplification.

4. Discussion

387

388

389

390

391

392

393

4.1. Formation of the B2 and σ phases at 700 °C

As shown in Fig. 4(a), the material after aging at 700 °C for 500 h is full of 394 needle-like B2 precipitates formed in the FCC matrix, and these precipitates are expected 395 to produce hardening. The chemical information shown in Figs. 4(b) and 4(c) 396 demonstrates that these B2 precipitates are of a NiAl-type. The similar morphology of the 397 B2 phase and its orientation relation with the parent FCC matrix have been reported in 398 399 several papers [19, 59, 60]. A Kurdjumov-Sachs (K-S) orientation relationship is present between the B2 precipitates and the FCC matrix [19, 59-61]. The large lattice misfit 400 $(\frac{a_{FCC,111}-a_{B2,110}}{a_{FCC,111}}\approx 19.9\%)$ between the FCC matrix and B2 phase indicates that the 401 402 interface between FCC and B2 phases is incoherent. Accordingly, it explains the reason why the needle-like B2 phase was precipitated in the FCC matrix because of the large 403 strain energy if it were round shaped. Due to the large lattice misfit, the effect of the 404 elastic strain energy becomes dominating the influence of the interfacial energy when the 405 B2 phase begins to precipitate. Thus, the needle-like B2 phase with the relatively large 406 interfacial energy was formed to relieve the large strain interaction between FCC and 407 BCC phases. 408

Combining the thermodynamic calculations (Fig. 2) with the APT results (Fig. 5), the Cr-rich precipitate of Al_{0.3}CoCrFeNi aged at 700 °C for 500 h is referred to be the σ phase. Through the detailed thermodynamic calculations (Fig. 2), the σ phase appears to be stable at intermediate temperatures, between 350 °C and 720 °C for Al_{0.3}CoCrFeNi. The formation of σ phase is observed in the Al_{0.3}CoCrFeNi is owing to the following reasons: first, Cr is known as a strong σ phase former, and the σ phase has also been shown to form in binary systems of the Cr-Co, Cr-Fe, and Cr-Ni [62]; second, other substitutional elements such as Al, Co, Fe, and Ni, having similar atomic radii with Cr, do not destabilize the σ phases for Al_{0.3}CoCrFeNi HEAs. The Co- and Cr-rich σ phases were also observed in the as-cast Al_{0.44}CoCrFeNi alloy by the Z-contrast technique in a scanning TEM (STEM) mode [63], in Al-Co-Cr-Fe-Ni alloys containing around 15 to 23 at.% Al [64], in Cr-Fe-Co-Ni-Al-Ti alloys [65], in CoCrFeMnNi at grain boundaries after annealing at 700 °C for 500 days [62], and stainless steels [66]. The hardness of the alloys increases with increasing the content of the σ phase in Fe-based composites [67]. However, the σ phases are known to deteriorate the ductility of materials at high temperatures. Thus, the understanding of the σ precipitation will allow for some control over the properties of HEAs in the future.

409

410

411

412

413

414

415

416

417

418

419

420

421

422

423

424

425

426

427

428

429

430

431

Figure 11(a) gives the schematic representation of the microstructure in the studied HEA after aging at 700 °C for 500 h. The aged HEA comprises the FCC matrix, needle-like B2 phase within grains, and granular σ phase along the grain boundary. To achieve an enhanced combination of strength and ductility, the future efforts should focus on the optimization of constituent phases in terms of the morphology and volume fraction through the integration of experiments and CALPHAD thermodynamic predictions.

4.2. Comparison between thermodynamic calculations and experimental results

432

433

434

435

436

437

438

439

440

441

442

443

444

445

446

447

448

449

450

451

452

453

454

The thermodynamically calculated results (Fig. 2) help us better understand the experimental results. It facilitates the identification of the NiAl-rich phase (Figs. 4(b) and 4(c)) and the Cr-rich phases (Figs. 5(a) and 5(b)) as the B2 and σ phase in Al_{0.3}CoCrFeNi, respectively. There are great agreements of the phase fractions between the measured and calculated values for Al_{0.3}CoCrFeNi. The experimental results show that the FCC phase fraction after homogenization at 1,250 °C for 2 hours is ~ 100 %, which agrees well with our calculated result (~ 100 %) accordingly. At 700 °C, the calculated phase fractions of FCC phase, B2 phase, and σ phase, are 85, 12, and 3 %, respectively (Fig. 2(b)), while our experimental results are about 86 and 14% for FCC and B2 phases, respectively (Figs. 4 (a)). Note that the σ phase is neglected when counting the volume fraction, because of its minor amount and the inadequate represented region in the SEM image (Fig. (4a)). One may also notice that there are some differences between the compositions predicted by CALPHAD (Fig. 2(b)) and those measured by APT (Figs. 3(b) and 4(c)) of FCC (1250 °C homogenized state) and B2 phases (700 °C aged state). For example, in the 1250 °C homogenized state, the measured concentrations of Fe and Al are about 27 at.% and 4.5 at.%, while the nominal concentration of Fe and Al should be ~23 at.% and 7 at.%. This difference could be due to the evaporation of Al element at that high temperature (1250 °C). Moreover, in the 700 °C aged state, the elemental concentrations in NiAl-type B2 phase predicted by CAPHAD (Al: 22.16 at.%, Co: 3.63 at.%, Cr: 0.69 at.%, Fe: 4.41 at.%, and Ni: 69.11%) are different from those measured by APT (Al: ~ 37 at.%, Co: ~ 12 at.%, Cr: ~ 2 at.%, Fe: ~ 8 at.%, and Ni: $\sim 42\%$). Such a discrepancy may be due to the inaccuracy of the current thermodynamic database, the non-equilibrium

state of B2 phase, or the selected area dependence of the SEM observations (Fig. 4(a)). Overall, the thermodynamic calculations provide basically accurate predictions on phase fractions, phase chemical compositions, etc., and effectively accelerate the new alloy design through adjusting heat-treatment processing parameters.

4.3. Elastic anisotropic behavior

Since there were no available experimental data for the single crystal elastic constants of Al_{0.3}CoCrFeNi, we estimated their elastic constants from the experimental polycrystalline neutron diffraction data. This calculation is of practical importance, because single crystal elastic constants are usually not available for newly designed alloys. The Al_{0.3}CoCrFeNi material is loaded uniaxially in the elastic regime, and each hkl-specific lattice strain as a function of the applied stress in the loading and transverse directions, respectively, is measured simultaneously using neutron diffraction (seen in Fig. 1). Then $1/E_{hkl}$ and v_{hkl}/E_{hkl} are calculated, using the Kroner model [68], by setting C_{ij} as free parameters from the following Equations (6) and (7). Finally, single crystal elastic constants, C_{ij} , are determined by the least squares fitting covering the different measured hkl directions, ranging from the (200), (220), (331), and (111) for Al_{0.3}CoCrFeNi after being aged at 700 °C for 500 h [Eq. (8)] [68].

$$\frac{1}{9K} - \frac{1}{6G_{bkl}} = -\frac{v_{hkl}}{E_{bkl}} \tag{6}$$

$$\frac{1}{G_{hkl}} = 2\left(\frac{1}{E_{hkl}} + \frac{v_{hkl}}{E_{hkl}}\right) \tag{7}$$

474
$$\chi^{2} = \sum_{i=1}^{n} \left(\left(\frac{1}{E_{hkl}} \right)_{\exp,i} - \left(\frac{1}{E_{hkl}} \right)_{\text{mod } el,i} \right)^{2} / e_{1,i}^{2} + \sum_{i=1}^{n} \left(\left(\frac{V_{hkl}}{E_{hkl}} \right)_{\exp,i} - \left(\frac{V_{hkl}}{E_{hkl}} \right)_{\text{mod } el,i} \right)^{2} / e_{2,i}^{2}$$
(8)

where K is the bulk modulus [= $(C_{11}+2C_{12})/3$]; E_{hkl} , v_{hkl} , and G_{hkl} are Young's modulus, Poisson's ratios, and shear moduli in the hkl direction, respectively; n is the number of (hkl) diffraction planes used to fit the Kroner model; then $(\frac{1}{E_{hkl}})_{exp}$ [the linear slopes of Bank 1 within Fig. 8(d)] and $(\frac{V_{hkl}}{E_{hkl}})_{exp}$ [the linear slopes of Bank 2 within Fig. 8(d)] are determined from the neutron diffraction; e_1 and e_2 are the corresponding experimental errors. The calculated elastic moduli, C11, C12, and C44 (listed in Table 1), is used for CPFEM. The calculated G (88 GPa) is for Section 4.4.

4.4. Strengthening effect of B2 Phase

The lattice strain versus stress relationship (Fig. 10(c)) provides key features in understanding the governing deformation mechanisms. Qualitatively, the splitting of lattice strains (Fig. 10(c)) indicates load sharing between the hard B2 phase and soft FCC phases. The in situ neutron lattice evolution of the specific {hkl} lattice strains of the FCC matrix and B2 phase as a function of average stress (Fig. 11(c)) shows that at 300 MPa, the slope of the FCC matrix is increased, relative to the linear elastic response, while the slope of the elastic strain of the B2 phase is reduced. This phenomenon directly proves that B2 is the strengthening phase. The increased linear slope of the FCC matrix indicates that the matrix cannot assume the further elastic strain and begins to plastically deform. Therefore, the yielding of the matrix leads to the plastic strain with the reduced rate of the increase of the elastic strain (i.e., lattice strain). In contrast, the reduced slope of the elastic strain of the precipitate reflects that the precipitate is still deforming

elastically, and the majority of the total strain is now transferred to the precipitate, which induces the decrease in the slope of the elastic strain of the precipitate.

The precipitation strengthening model is proposed to relate the size and volume fraction of precipitates with mechanical properties of the Al_{0.3}CoCrFeNi alloy. Two main deformation mechanisms, either through a dislocation bypass (Orowan-type) or particle shearing mechanism [69, 70], exist for precipitation hardening. Shearing mechanism is more common when precipitates are coherent and small, whereas Orowan bypassing mechanism generally occurs when precipitates are large or incoherent with the matrix. After aging at 700 °C for 500 h, the needle-like B2 precipitates become much large with an average width and length of 162 and 652 nm, respectively, which cannot be sheared anymore. Thus, the dislocation in Al_{0.3}CoCrFeNi can only bypass through looping around them. This trend leaves an Orowan loop around the precipitates, which enhances the mechanical properties of the Al_{0.3}CoCrFeNi alloy. When the B2 precipitates behave like non-shearable particles, the mean precipitates (obstacle) strengthening, which is defined as the interaction force between the obstacle and the dislocation, is given by the following equation [71],

$$F = 2\beta Gb^2 \tag{9}$$

where β is a constant close to 0.5, G is shear modulus [\sim 88 GPa (calculated in Section. 4.3)] of the FCC matrix, b is the Burgers' vector of the dislocation within the FCC matrix.

For non-shearable B2 precipitates (the shape of B2 is shown in Fig. 11(b)), the effective obstacle spacing is the center-to-center distance between precipitates, L, which can approximately use the position relation in the Al-Mg-Si alloy [72].

$$L = \left(\frac{2\pi}{f_{PA}}\right)^{1/2} < r > \tag{10}$$

where f_{PA} is the volume fraction of the B2 precipitates, while $\langle r \rangle$ is the cylindrical radius of the B2 precipitates.

Thus, the contribution of B2 precipitates to the strength through aging, as shown below [71],

$$\sigma_{ppt} = 2\beta GbM \left(\frac{f_{PA}}{2\pi}\right)^{1/2} \frac{1}{\langle r \rangle}$$
 (11)

where M is Taylor factor. The final strengthening increment from the B2 precipitation, σ_{ppt}^{cal} is determined to be 126 MPa, using $\beta = 0.5$, G = 88 GPa (calculated in Section. 4.3), $b = \sqrt{2} \times a_{FCC} / 2 = 0.2535$ nm, M = 3.06, $\langle r \rangle = 81$ nm, and $f_{PA} = 0.14$, which is close to the experimental results of $\sigma_{ppt}^{exp} = 300 - 145 = 155$ MPa. The minor different (~ 29 MPa) could be attributed to the strengthening contribution from the σ phase precipitated along grain boundaries (see Fig. 4(a)).

In the present study, both the homogenized and aged Al_{0.3}CoCrFeNi HEAs have an extremely large grain size (> 600 μm) [73]. According to the reported Hall-Petch constant of this alloy (~ 824 MPa/μm^{0.5}) [19], the contribution from the grain-boundary strengthening (< 33 MPa) can be neglected. Therefore, it is not surprising to observe much higher yield strength in other reported Al_{0.3}CoCrFeNi alloys that have very finer grain sizes leading to the remarkable grain-boundary strengthening effect [18, 19, 22, 23]. The precipitation strengthening from the B2 phase is the main reason causing the

enhancement of the yield strength of this alloy after aging at 700 °C for 500 h. The experimental value of the precipitation strengthening of the B2 precipitates is about 155 MPa, which is much higher than that reported by Gwalani et al ($\Delta\sigma_{B2}\sim56$ MPa) and by Yasuda et al [19, 54]. The strengthening difference can be attributed to the volume fraction and morphology of B2 precipitates. If the volume fraction of B2 precipitates is small or B2 mainly precipitates along the grain boundaries, the effect of precipitation strengthening will become weak.

5. Conclusions

In summary, we have studied (1) the phase stability of Al_{0.3}CoCrFeNi HEA after heat treatments and (2) the deformation mechanisms of the single-phase and multiphase Al_{0.3}CoCrFeNi HEAs. Comprehensive approaches by both experiments (APT and in situ neutron aided tensile tests) and theoretical prediction (thermodynamic calculations and crystal-plasticity finite-element modeling) have been used jointly for drawing the following conclusions:

- (1). New alloys with the balanced yield strength and ductility have been designed. After two-step heat treatments (homogenized at 1,250 °C for 2 hours and aged at 700 °C for 500 hours) with the assistance of thermodynamic calculations, the optimal microstructure combinations, the FCC matrix, needle-like B2 phase within grains, and granular σ phase along the grain boundary, is achieved for Al_{0.3}CoCrFeNi.
- (2). In situ neutron diffraction experiments were conducted to study the strengthening effect of the B2 phase on tensile properties of Al_{0.3}CoCrFeNi HEAs directly. The results show that the heat treatment introduces the secondary B2 phase into

the FCC matrix, which increases the yield strength from 145 MPa to 300 MPa. During tensile deformation, the reduced slope of the elastic strain of the B2 phase reflects that the precipitate is still deforming elastically, and the additional plastic strain from the FCC matrix is transferred to the B2 phase.

- (3). The Orowan bypass mechanism is expected to take the strengthening control in Al_{0.3}CoCrFeNi after aging at 700 °C for 500 h, when the B2 particles are incoherent with the FCC matrix. The stress increment (126 MPa), calculated based on the Orowan theory, is close to the experimental results (155 MPa).
- (4). The phase stability and strengthening mechanisms of both single-phase and multi-phase HEAs has been fundamentally understood through the integration of experimental and theoretical approaches, which can provide insights for the discovery and development of other engineering materials in the future.

Acknowledgments

H. Diao and P.K. Liaw would like to acknowledge the Department of Energy (DOE), Office of Fossil Energy, National Energy Technology Laboratory (DE-FE-0008855, DE-FE-0024054 and DE-FE-0011194) with Mr. V. Cedro, Mr. R. Dunst, and Dr. J. Mullen as program managers. R. Feng and P.K. Liaw appreciate the support of the U.S. Army Research Office project (W911NF-13-1-0438) with the program manager, Dr. M.P. Bakas, Dr. N.S. Mathaudhu, and Dr. D.M. Stepp. R. Feng and P.K. Liaw also thank the support from the National Science Foundation (DMR 1611180 and 1809640) with the program directors, Dr. G. Shiflet and Dr. D. Farkas. P.K. Liaw and Y. Gao appreciate the support of the Center for Materials Processing (CMP) with Dr. C.J. Rawn as the director.

APT was conducted at the ORNL's Center for Nanophase Materials Sciences (CNMS), which is a U.S. DOE Office of Science User Facility. The neutron diffraction experiment was carried out on the VULCAN diffractometer at the ORNL's Spallation Neutron Source sponsored by the Scientific User Facilities Division, the Office of Basic Energy Sciences, U.S. Department of Energy. T. Liu and Y. Gao were supported by the U.S. Department of Energy, Office of Science, Basic Energy Sciences, Materials Sciences and Engineering Division.

590 [2] J.W. Yeh, S.K. Chen, S.J. Lin, J.Y. Gan, T.S. Chin, T.T. Shun, C.H. Tsau, S.Y. Chang, Nanostructured high-entropy alloys with multiple principal elements: novel alloy design concepts and outcomes, Adv. Eng. Mater. 6(5) (2004) 299-303.

- 593 [3] Y. Zhang, T.T. Zuo, Z. Tang, M.C. Gao, K.A. Dahmen, P.K. Liaw, Z.P. Lu, 594 Microstructures and properties of high-entropy alloys, Prog. Mater. Sci. 61 (2014) 595 1-93.
- 596 [4] M.C. Gao, J.W. Yeh, P.K. Liaw, Y. Zhang, High-entropy Alloys: Fundamental and Applications, Springer International Publishing, Cham, Switzerland2016.
- 598 [5] D.B. Miracle, O.N. Senkov, A critical review of high entropy alloys and related concepts, Acta Mater. 122 (2017) 448-511.
- 600 [6] O.N. Senkov, J.D. Miller, D.B. Miracle, C. Woodward, Accelerated exploration 601 of multi-principal element alloys with solid solution phases, Nat. Commun. 6 602 (2015) 6529.
- 603 [7] H.Y. Diao, R. Feng, K.A. Dahmen, P.K. Liaw, Fundamental deformation 604 behavior in high-entropy alloys: An overview, Curr. Opin. Solid State Mater. Sci. 605 21(5) (2017) 252-266.
- A. Gali, E.P. George, Tensile properties of high- and medium-entropy alloys, Intermetallics 39 (2013) 74-78.
- F. Otto, A. Dlouhý, C. Somsen, H. Bei, G. Eggeler, E.P. George, The influences of temperature and microstructure on the tensile properties of a CoCrFeMnNi high-entropy alloy, Acta Mater. 61(15) (2013) 5743-5755.
- 511 [10] J.Y. He, W.H. Liu, H. Wang, Y. Wu, X.J. Liu, T.G. Nieh, Z.P. Lu, Effects of Al addition on structural evolution and tensile properties of the FeCoNiCrMn highentropy alloy system, Acta Mater. 62 (2014) 105-113.
- 614 [11] Z. Wu, Y. Gao, H. Bei, Thermal activation mechanisms and Labusch-type 615 strengthening analysis for a family of high-entropy and equiatomic solid-solution 616 alloys, Acta Mater. 120 (2016) 108-119.
- [12] Z. Wu, Y.F. Gao, H. Bei, Single crystal plastic behavior of a single-phase, face center-cubic-structured, equiatomic FeNiCrCo alloy, Scripta Mater. 109 (2015)
 108-112.
- 620 [13] M.A. Hemphill, T. Yuan, G.Y. Wang, J.W. Yeh, C.W. Tsai, A. Chuang, P.K. Liaw, Fatigue behavior of Al0.5CoCrCuFeNi high entropy alloys, Acta Mater. 60(16) (2012) 5723-5734.
- 623 [14] M. Seifi, D. Li, Z. Yong, P.K. Liaw, J.J. Lewandowski, Fracture toughness and fatigue crack growth behavior of as-cast high-entropy alloys, JOM 67(10) (2015) 2288-2295.
- Example 15 In Indian Problem Indian Indian
- 629 [16] K.V.S. Thurston, B. Gludovatz, A. Hohenwarter, G. Laplanche, E.P. George, R.O. Ritchie, Effect of temperature on the fatigue-crack growth behavior of the highentropy alloy CrMnFeCoNi, Intermetallics 88 (2017) 65-72.

- 632 [17] B. Gludovatz, A. Hohenwarter, D. Catoor, E.H. Chang, E.P. George, R.O. Ritchie, A fracture-resistant high-entropy alloy for cryogenic applications, Science 345(6201) (2014) 1153-1158.
- S. Gangireddy, B. Gwalani, R.S. Mishra, Grain size dependence of strain rate sensitivity in a single phase FCC high entropy alloy Al0.3CoCrFeNi, Mater. Sci. Eng. A 736 (2018) 344-348.
- 638 [19] B. Gwalani, V. Soni, M. Lee, S.A. Mantri, Y. Ren, R. Banerjee, Optimizing the coupled effects of Hall-Petch and precipitation strengthening in a Al0.3CoCrFeNi high entropy alloy, Mater. Des. 121 (2017) 254-260.
- [20] G.A. Salishchev, M.A. Tikhonovsky, D.G. Shaysultanov, N.D. Stepanov, A.V.
 Kuznetsov, I.V. Kolodiy, A.S. Tortika, O.N. Senkov, Effect of Mn and V on
 structure and mechanical properties of high-entropy alloys based on CoCrFeNi
 system, J. Alloys Compd. 591 (2014) 11-21.
- J. He, H. Wang, H. Huang, X. Xu, M. Chen, Y. Wu, X. Liu, T. Nieh, K. An, Z. Lu,
 A precipitation-hardened high-entropy alloy with outstanding tensile properties,
 Acta Mater. 102 (2016) 187-196.
- [22] B. Gwalani, S. Gorsse, D. Choudhuri, M. Styles, Y. Zheng, R.S. Mishra, R. Banerjee, Modifying transformation pathways in high entropy alloys or complex concentrated alloys via thermo-mechanical processing, Acta Mater. 153 (2018) 169-185.
- 652 [23] K. Liu, M. Komarasamy, B. Gwalani, S. Shukla, R.S. Mishra, Fatigue behavior of 653 ultrafine grained triplex Al0.3CoCrFeNi high entropy alloy, Scripta Mater. 158 654 (2019) 116-120.
- 655 [24] H. Diao, L.J. Santodonato, Z. Tang, T. Egami, P.K. Liaw, Local structures of 656 high-entropy alloys (HEAs) on atomic scales: an overview, JOM 67(10) (2015) 657 2321-2325.
- [25] X.D. Xu, P. Liu, S. Guo, A. Hirata, T. Fujita, T.G. Nieh, C.T. Liu, M.W. Chen,
 Nanoscale phase separation in a fcc-based CoCrCuFeNiAl0.5 high-entropy alloy,
 Acta Mater. 84 (2015) 145-152.
- 561 [26] S. Singh, N. Wanderka, B.S. Murty, U. Glatzel, J. Banhart, Decomposition in multi-component AlCoCrCuFeNi high-entropy alloy, Acta Mater. 59(1) (2011) 182-190.
- 664 [27] B.A. Welk, R.E. Williams, G.B. Viswanathan, M.A. Gibson, P.K. Liaw, H.L. Fraser, Nature of the interfaces between the constituent phases in the high entropy alloy CoCrCuFeNiAl, Ultramicroscopy 134 (2013) 193-199.
- 667 [28] M.V. Ivchenko, V.G. Pushin, N. Wanderka, High-entropy equiatomic 668 AlCrFeCoNiCu alloy: Hypotheses and experimental data, Tech. Phys. 59(2) 669 (2014) 211-223.
- [29] L.J. Santodonato, Y. Zhang, M. Feygenson, C.M. Parish, M.C. Gao, R.J. Weber,
 J.C. Neuefeind, Z. Tang, P.K. Liaw, Deviation from high-entropy configurations
 in the atomic distributions of a multi-principal-element alloy, Nat. Commun. 6
 (2015) 5964.
- K.G. Pradeep, N. Wanderka, P. Choi, J. Banhart, B.S. Murty, D. Raabe, Atomicscale compositional characterization of a nanocrystalline AlCrCuFeNiZn highentropy alloy using atom probe tomography, Acta Mater. 61(12) (2013) 4696-4706.

- 678 [31] A. Manzoni, H. Daoud, R. Volkl, U. Glatzel, N. Wanderka, Phase separation in equiatomic AlCoCrFeNi high-entropy alloy, Ultramicroscopy 132 (2013) 212-5.
- 680 [32] C.C. Tasan, Y. Deng, K.G. Pradeep, M.J. Yao, H. Springer, D. Raabe, 681 Composition Dependence of Phase Stability, Deformation mechanisms, and 682 mechanical properties of the CoCrFeMnNi high-entropy alloy system, JOM 66(10) 683 (2014) 1993-2001.
- 684 [33] M.J. Yao, K.G. Pradeep, C.C. Tasan, D. Raabe, A novel, single phase, nonequiatomic FeMnNiCoCr high-entropy alloy with exceptional phase stability and tensile ductility, Scripta Mater. 72–73 (2014) 5-8.
- 687 [34] M. Laurent-Brocq, A. Akhatova, L. Perrière, S. Chebini, X. Sauvage, E. Leroy, Y. Champion, Insights into the phase diagram of the CrMnFeCoNi high entropy alloy, Acta Mater. 88 (2015) 355-365.
- E.W. Huang, D. Yu, J.-W. Yeh, C. Lee, K. An, S.-Y. Tu, A study of lattice elasticity from low entropy metals to medium and high entropy alloys, Scripta Mater. 101 (2015) 32-35.
- 693 [36] Y. Wu, W.H. Liu, X.L. Wang, D. Ma, A.D. Stoica, T.G. Nieh, Z.B. He, Z.P. Lu, In-situ neutron diffraction study of deformation behavior of a multi-component high-entropy alloy, Appl. Phys. Lett. 104(5) (2014) 051910.
- 696 [37] M.C. Gao, D.E. Alman, Searching for next single-phase high-entropy alloy compositions, Entropy 15(10) (2013) 4504-4519.
- 698 [38] C. Zhang, F. Zhang, S. Chen, W. Cao, Computational thermodynamics aided high-entropy alloy design, Jom 64(7) (2012) 839-845.
- F. Zhang, C. Zhang, S.L. Chen, J. Zhu, W.S. Cao, U.R. Kattner, An understanding of high entropy alloys from phase diagram calculations, Calphad 45 (2014) 1-10.
- 702 [40] C. Zhang, F. Zhang, H. Diao, M.C. Gao, Z. Tang, J.D. Poplawsky, P.K. Liaw, Understanding phase stability of Al-Co-Cr-Fe-Ni high entropy alloys, Mater. Des. 109 (2016) 425-433.
- C. Zhang, M.C. Gao, CALPHAD Modeling of High-Entropy Alloys, in: M.C.
 Gao, J.W. Yeh, P.K. Liaw, Y. Zhang (Eds.), High-entropy Alloys: Fundamental and Applications, Springer International Publishing, Cham, Switzerland2016, pp. 399-444.
- R. Feng, M.C. Gao, C. Zhang, W. Guo, J.D. Poplawsky, F. Zhang, J.A. Hawk, J.C.
 Neuefeind, Y. Ren, P.K. Liaw, Phase stability and transformation in a light-weight high-entropy alloy, Acta Mater. 146 (2018) 280-293.
- 712 [43] R. Feng, M.C. Gao, C. Lee, M. Mathes, T. Zuo, S. Chen, J.A. Hawk, Y. Zhang, P.K. Liaw, Design of light-weight high-entropy alloys, Entropy 18(9) (2016) 333.
- 714 [44] S. Huang, Y. Gao, K. An, L. Zheng, W. Wu, Z. Teng, P.K. Liaw, Deformation 715 mechanisms in a precipitation-strengthened ferritic superalloy revealed by in situ 716 neutron diffraction studies at elevated temperatures, Acta Mater. 83 (2015) 137-717 148.
- 718 [45] W. Guo, D.A. Garfinkel, J.D. Tucker, D. Haley, G.A. Young, J.D. Poplawsky, An 719 atom probe perspective on phase separation and precipitation in duplex stainless 720 steels, Nanotechnology 27(25) (2016) 254004.
- 721 [46] D. Ma, A.D. Stoica, X.L. Wang, Z.P. Lu, M. Xu, M. Kramer, Efficient local atomic packing in metallic glasses and its correlation with glass-forming ability, Phys. Rev. B 80(1) (2009).

- 724 [47] X.L. Wang, T.M. Holden, G.Q. Rennich, A.D. Stoica, P.K. Liaw, H. Choo, C.R. Hubbard, VULCAN—The engineering diffractometer at the SNS, Physica B: Condensed Matter 385-386(Part 1) (2006) 673-675.
- 727 [48] Z.K. Teng, F. Zhang, M.K. Miller, C.T. Liu, S. Huang, Y.T. Chou, R.H. Tien, Y.A. Chang, P.K. Liaw, Thermodynamic modeling and experimental validation of the Fe-Al-Ni-Cr-Mo alloy system, Mater. Lett. 71 (2012) 36-40.
- 730 [49] D. Peirce, R. Asaro, A. Needleman, An analysis of nonuniform and localized deformation in ductile single crystals, Acta Metall. 30(6) (1982) 1087-1119.
- 732 [50] C. Pu, Y. Gao, Crystal plasticity analysis of stress partitioning mechanisms and their microstructural dependence in advanced steels, J. Appl. Mech. 82(3) (2015) 031003.
- 735 [51] A.F. Bower, E. Wininger, A two-dimensional finite element method for simulating 736 the constitutive response and microstructure of polycrystals during high 737 temperature plastic deformation, J. Mech. Phys. Solids 52(6) (2004) 1289-1317.
- [52] L.L. Zheng, Y.F. Gao, S.Y. Lee, R.I. Barabash, J.H. Lee, P.K. Liaw, Intergranular strain evolution near fatigue crack tips in polycrystalline metals, J. Mech. Phys. Solids 59(11) (2011) 2307-2322.
- 741 [53] M.P. Moody, L.T. Stephenson, A.V. Ceguerra, S.P. Ringer, Quantitative binomial distribution analyses of nanoscale like-solute atom clustering and segregation in atom probe tomography data, Micros. Res. Tech. 71(7) (2008) 542-550.
- 744 [54] H.Y. Yasuda, H. Miyamoto, K. Cho, T. Nagase, Formation of ultrafine-grained 745 microstructure in Al0.3CoCrFeNi high entropy alloys with grain boundary 746 precipitates, Mater. Lett. 199 (2017) 120-123.
- 747 [55] Y. Zhang, J.P. Liu, S.Y. Chen, X. Xie, P.K. Liaw, K.A. Dahmen, J.W. Qiao, Y.L. Wang, Serration and noise behaviors in materials, Prog. Mater. Sci. (2017) 358-460.
- 750 [56] S. Chen, X. Xie, W. Li, R. Feng, B. Chen, J. Qiao, Y. Ren, Y. Zhang, K.A. Dahmen, P.K. Liaw, Temperature effects on the serrated behavior of an Al0.5CoCrCuFeNi high-entropy alloy, Mater. Chem. Phys. 210 (2018) 20-28.
- 753 [57] E. Kröner, Berechnung der elastischen Konstanten des Vielkristalls aus den Konstanten des Einkristalls, Z. Phys. 151 (1958) 504-518.
- [58] G.H. Thomas, C.B. Paul, J.P. Henry, Calculation of Single-Crystal Elastic
 Constants for Cubic Crystal Symmetry from Powder Diffraction Data, J. Appl.
 Crystallogr. 31 (1998) 929-935.
- 758 [59] T.-T. Shun, Y.-C. Du, Microstructure and tensile behaviors of FCC Al0.3CoCrFeNi high entropy alloy, J. Alloys Compd. 479(1) (2009) 157-160.
- [60] B. Gwalani, V. Soni, D. Choudhuri, M. Lee, J.Y. Hwang, S.J. Nam, H. Ryu, S.H.
 Hong, R. Banerjee, Stability of ordered L12 and B2 precipitates in face centered
 cubic based high entropy alloys Al0.3CoFeCrNi and Al0.3CuFeCrNi2, Scripta
 Mater. 123 (2016) 130-134.
- 764 [61] H.Y. Yasuda, H. Miyamoto, K. Cho, T. Nagase, Formation of ultrafine-grained 765 microstructure in Al0.3CoCrFeNi high entropy alloys with grain boundary 766 precipitates, Mater. Lett. 199 (2017) 120-123.
- [62] F. Otto, A. Dlouhý, K.G. Pradeep, M. Kuběnová, D. Raabe, G. Eggeler, E.P.
 George, Decomposition of the single-phase high-entropy alloy CrMnFeCoNi after
 prolonged anneals at intermediate temperatures, Acta Mater. 112 (2016) 40-52.

- 770 [63] T.M. Butler, J.P. Alfano, R.L. Martens, M.L. Weaver, High-temperature oxidation 771 behavior of Al-Co-Cr-Ni-(Fe or Si) multicomponent high-entropy alloys, JOM 67 772 (2015) 246-259.
- 773 [64] W.R. Wang, W.L. Wang, S.C. Wang, Y.C. Tsai, C.H. Lai, J.W. Yeh, Effects of Al addition on the microstructure and mechanical property of AlxCoCrFeNi highentropy alloys, Intermetallics 26 (2012) 44-51.
- 776 [65] V.K. Portnoi, A.V. Leonov, S.E. Filippova, A.N. Streletskii, A.I. Logacheva, 777 Mechanochemical synthesis and heating-induced transformations of a high-778 entropy Cr-Fe-Co-Ni-Al-Ti alloy, Inorg. Mater. 50 (2014) 1202-1211.
- 779 [66] C.-C. Hsieh, W. Wu, Overview of intermetallic sigma phase precipitation in stainless steels, ISRN Metall.2012 (2012) 1-16.
- 781 [67] S.O. Yilmaz, M. Aksoy, C. Ozel, P. H., M. Gur, Effect of FeCr intermetallic on wear resistance of Fe-based composites, InTech2013, Chapter 1.
- [68] Z. Wang, A.D. Stoica, D. Ma, A.M. Beese, Diffraction and single-crystal elastic
 constants of Inconel 625 at room and elevated temperatures determined by neutron
 diffraction, Mater. Sci. Eng. A 674 (2016) 406-412.
- 786 [69] E. Orowan, Discussion in The Symposium on Internal Stresses in Metals and Alloys, Inst, Metals, London 451 (1948).
- 788 [70] A.J. Ardell, Precipitation hardening, Metall. Trans. A 16(12) (1985) 2131-2165.
- 789 [71] S. Esmaeili, D.J. Lloyd, W.J. Poole, A yield strength model for the Al-Mg-Si-Cu alloy AA6111, Acta Mater. 51(8) (2003) 2243-2257.
- 791 [72] J.F. Nie, B.C. Muddle, I.J. Polmear, The effect of precipitate shape and orientation 792 on dispersion strengthening in high strength aluminium alloys, Mater. Sci. Forum, 793 Trans Tech Publ, 1996, pp. 1257-1262.
- 794 [73] H. Diao, Experimental and Computational Investigation of High Entropy Alloys 795 for Elevated-Temperature Applications, PhD Thesis, University of Tennnessee 796 (2017).

797

798

799

800

801

802

803

Table Captions

804

809

- Table 1 Input material parameters for FCC and B2 phases in the crystal-plasticity finiteelement simulation (CPFEM) of the lattice strain evolution during tension at RT. Material
- 1 is the Al_{0.3}CoCrFeNi after homogenization at 1,250 °C for 2 h, and Material 2 is the
- 808 Al_{0.3}CoCrFeNi after aging at 700 °C for 500 h).

Figure Captions

- 810 Fig. 1 Schematic of the sample dimension (unit in mm) and position for neutron
- 811 diffraction measurements of lattice strain distributions during in situ tensile loading for
- the Al_{0.3}CoCrFeNi HEA. The beam size is 5 mm.
- Fig. 2 Thermodynamic Calculation of the Al_{0.3}CoCrFeNi HEA. (a) Calculated phase
- diagram in the temperature range from 200 °C to 1,500 °C. (b) Stable phases, phase
- fractions, and phase chemical compositions at two annealing temperatures.
- Fig. 3 APT analysis of the Al_{0.3}CoCrFeNi alloy after annealing at 1,250 °C for 2 hours. (a)
- 3D reconstruction of a $35 \times 35 \times 75$ nm³ volume, showing a homogeneous distribution of
- 818 all constituted elements, Al, Co, Cr, Fe, and Ni; (b) One-dimensional chemical
- 819 concentration profile along the arrowed direction in a; (c) Binominal frequency
- distribution analysis of all alloying elements, Al, Co, Cr, Fe, and Ni.
- Fig. 4 Microstructures with grains of Al_{0.3}CoCrFeNi after the heat treatment at 700 °C for
- 822 500 h. (a) SEM image. Needle-like second phases (white) appear in the FCC matrix
- 823 (Black). (c) Elemental profiles across the second phase along the black arrow in (b), as
- obtained from the APT data.

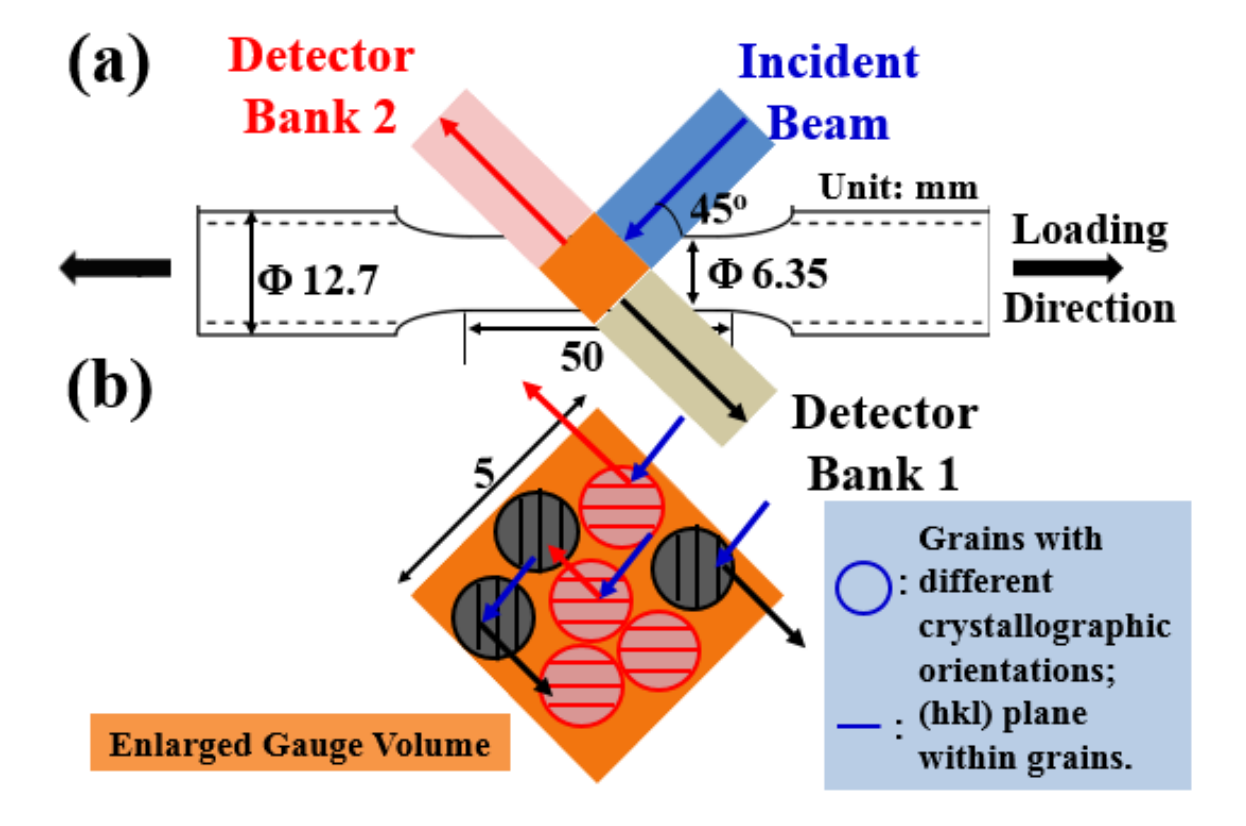
- Fig. 5 Microstructure along the grain boundary after aging at 700 °C for 500 hours of the
- 826 Al_{0.3}CoCrFeNi. (a) Elemental maps showing that the Cr-rich cluster (in the left-hand
- corner) in the FCC matrix. (b) Concentrations of the elements, Al, Co, Cr, Fe, and Ni,
- along the interface (30 at. % Cr) between the FCC matrix and σ phase. The error bars
- 829 represent the 2σ standard deviation.
- 830 Fig. 6 The full engineering stress-strain curves of the Al_{0.3}CoCrFeNi HEA alloy after
- homogenization at 1,250 °C for 2 hours (a) and after aging at 700 °C for 500 hours (b).
- Fig. 7 Neutron diffraction pattern of the Al_{0.3}CoCrFeNi HEA alloy after homogenization
- at 1,250 °C for 2 hours. (a) Tensile stress-strain curve; (b) neutron diffraction pattern,
- detected by the Bank 1 Detector. (b) neutron diffraction pattern, detected by the Bank 2
- Detector; and (d) evolution of lattice strain of the current HEA as a function of applied
- stress during tension.
- Fig. 8 Neutron diffraction pattern of the Al_{0.3}CoCrFeNi HEA alloy after aging at 700 °C
- for 500 hours. (a) Tensile stress-strain curve; (b) neutron diffraction pattern, detected by
- the Bank 1 Detector. (c) neutron diffraction pattern, detected by the Bank 2 Detector; and
- 840 (d) evolution of lattice strains of the current HEA as a function of applied stress during
- 841 tension.
- 842 Fig. 9 The finite element simulation is conducted on a tension specimen after
- 843 homogenization at 1,250 °C for 2 hours with cubic elements in the ABAQUS model.
- Refer to Alloy 1 in Table 1. Each grain of (a) is represented by 8 cubic elements in the
- overall setup in (b). The lattice strain evolution is given in (c).

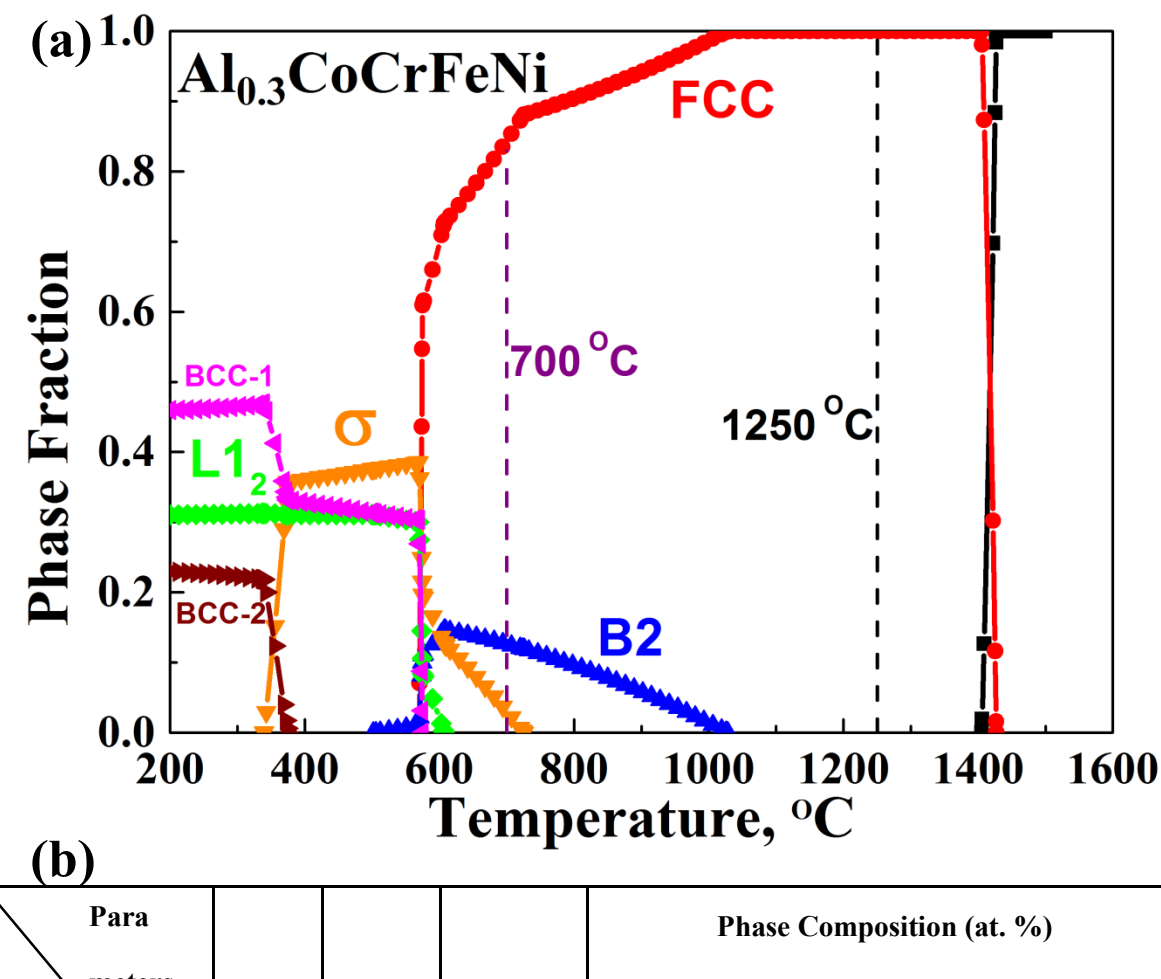
846 Fig. 10 The finite element simulation is conducted on a tension specimen after aging at 700 °C for 500 h with cubic elements in the ABAQUS model. Refer to Alloy 2 in Table 1. 847 (a) Needle-like second phase (purple) is represented in each grain. (b) The entire model 848 of polycrystals with cubic elements. (c) Lattice strain evolutions for the two phases with 849 respect to a number of grain families. 850 Fig. 11 The schematic representation of the newly designed HEAs with the balanced 851 yield strength and ductility after aging at 700 °C for 500 h. (a) material configurations, 852 comprising the FCC matrix, needle-like B2 phase within grains, and granular σ phase 853 along the grain boundary; (b) cylindrical morphology for the B2 phase, where the aspect 854 ratio (A) of the precipitate is defined as A = h/r. 855

856

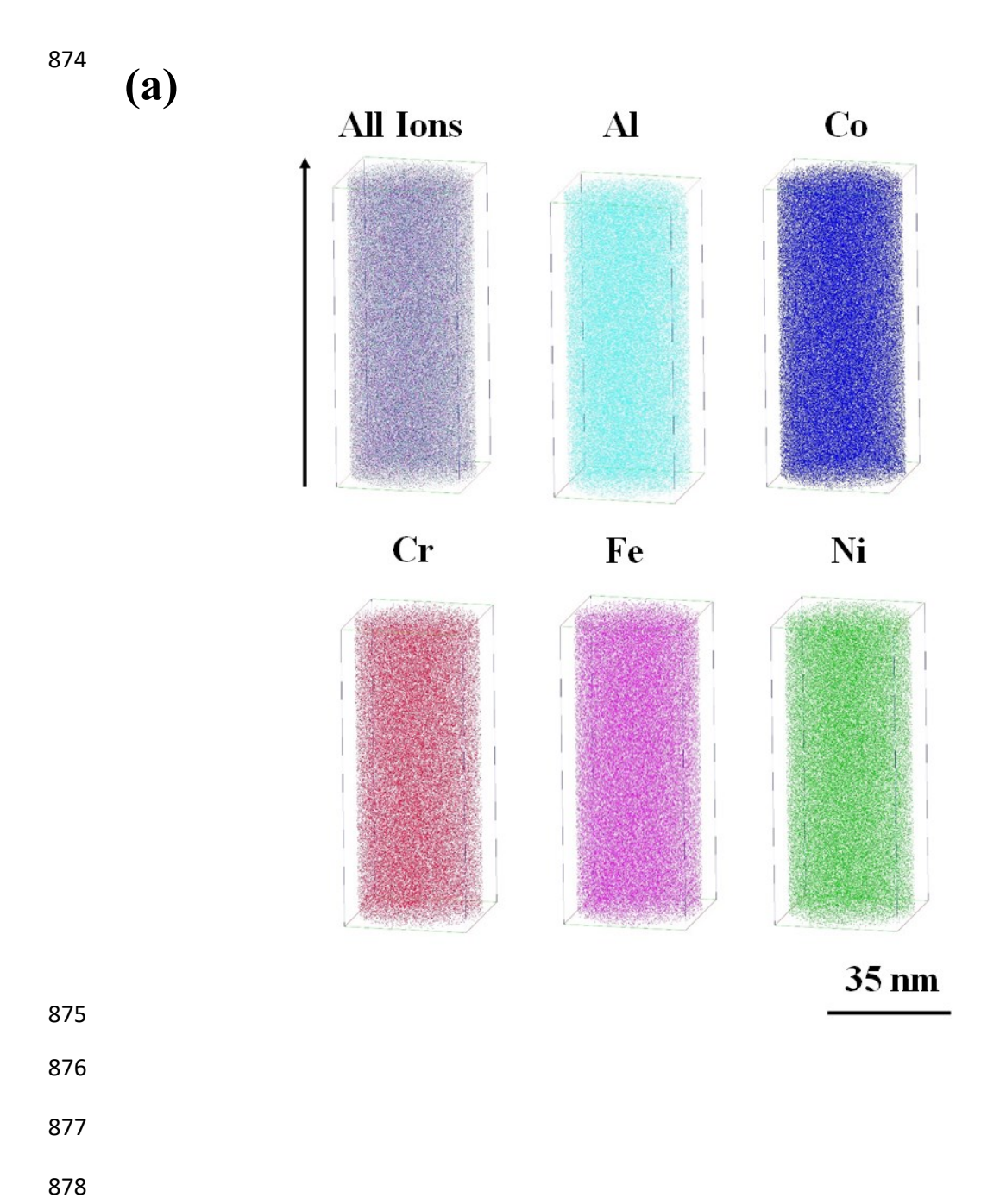
Table 1

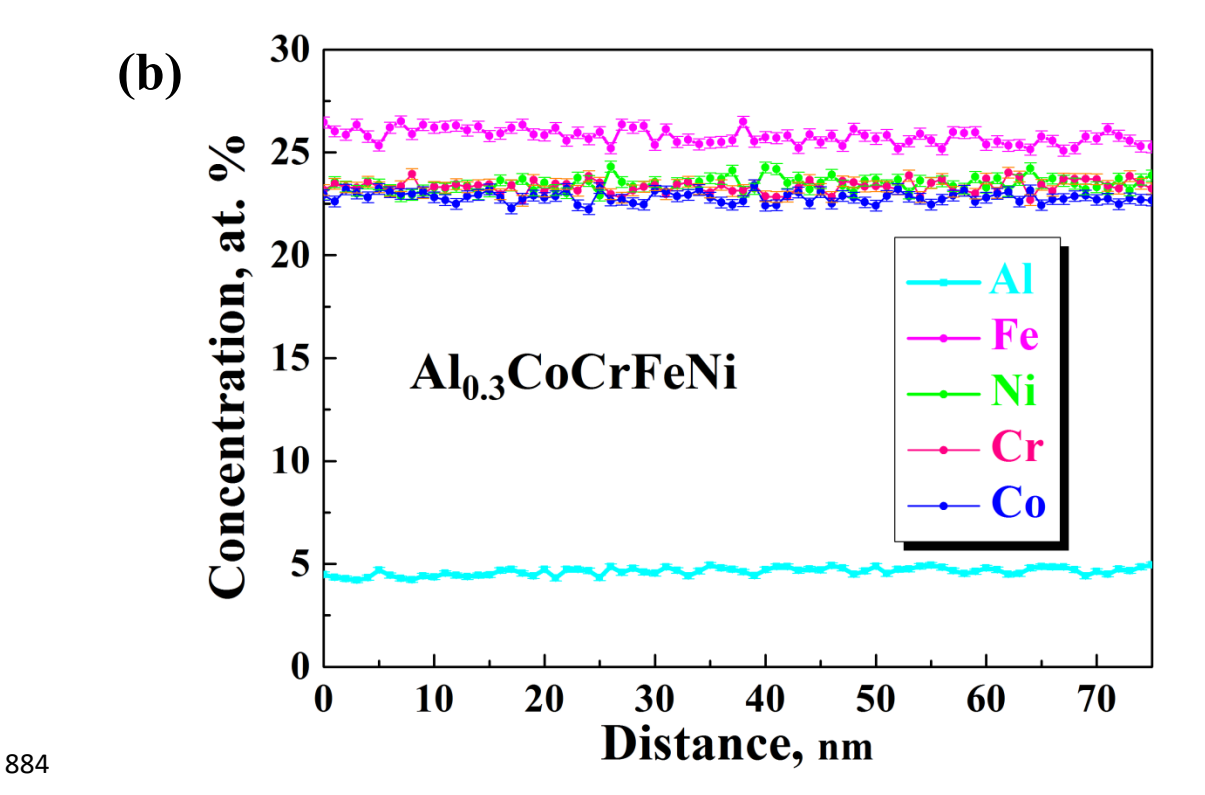
Material	Phases	C ₁₁ (GPa)	C ₁₂ (GPa)	C ₄₄ (GPa)	n	h ₀ (MPa)	τ _s (MPa)	τ ₀ (MPa)	q
1	FCC	229	168	122	10	85	185	44	1.0
2	FCC	210	165	129	10	1,000	630	120	1.0
	B2	220	151	90	10	-	-	-	-





Para		Stable Phase	Fraction (%)	Phase Composition (at. %)					
Meters	T (°C)			Al	Со	Cr	Fe	Ni	
	1,250	FCC	100	6.976	23.256	23.256	23.256	23.256	
Al _{0.3} CoCrFeNi		FCC	85	0.276	40.480	8.466	47.902	2.876	
	700	B2	12	22.160	3.632	0.689	4.414	69.106	
		σ	3	0.016	25.112	54.240	18.277	0.236	





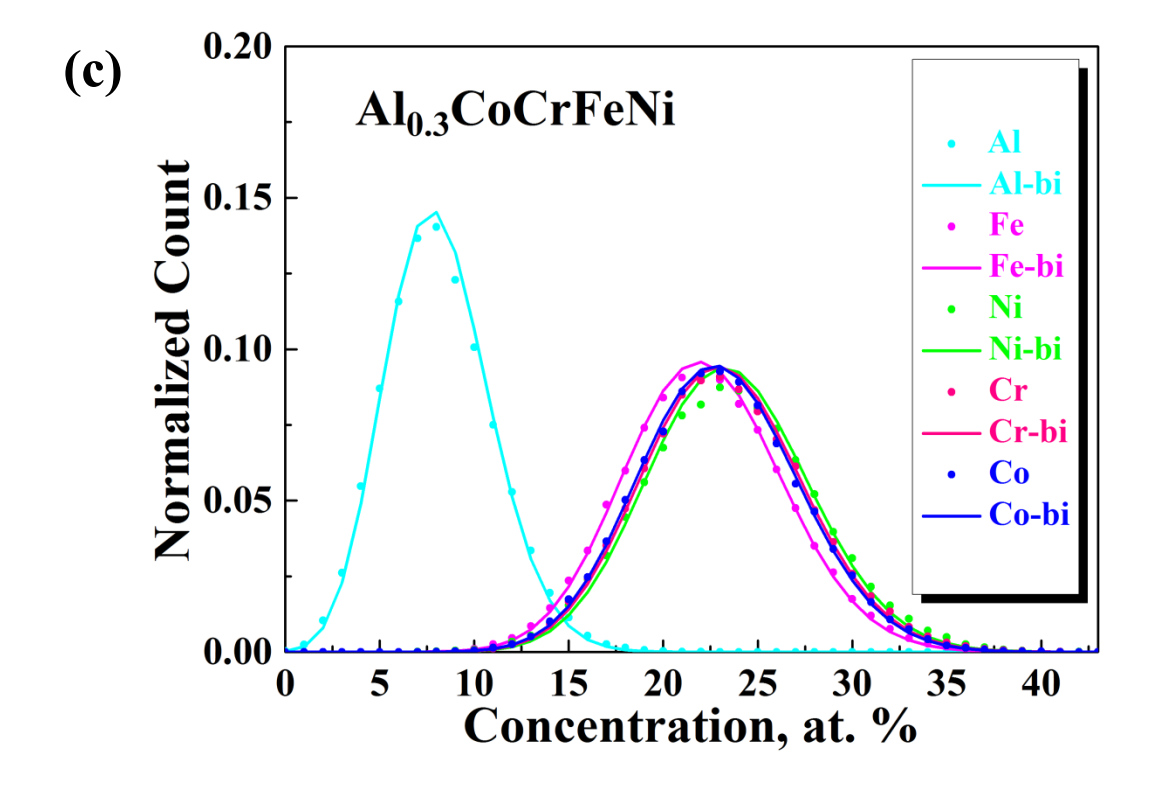
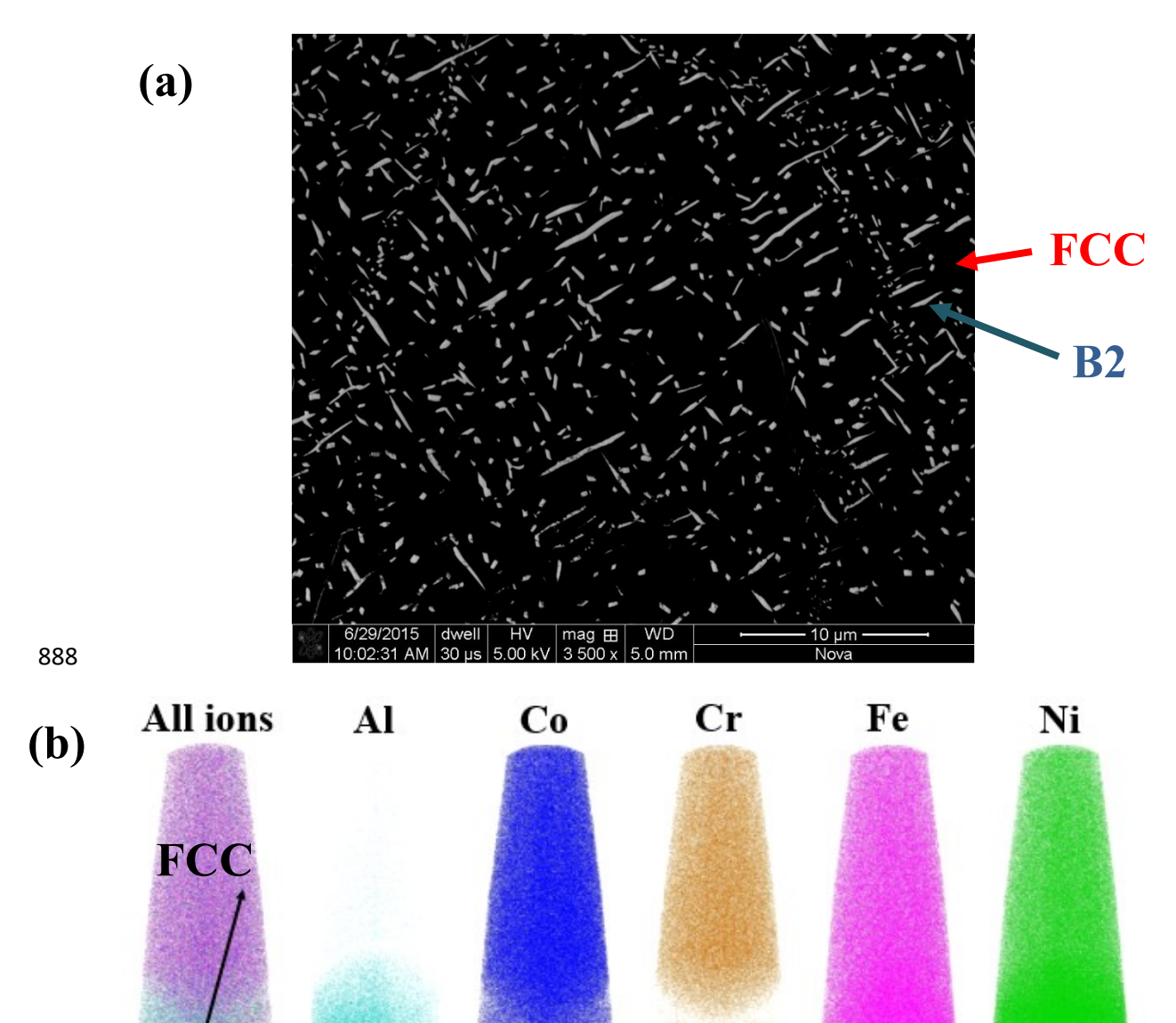


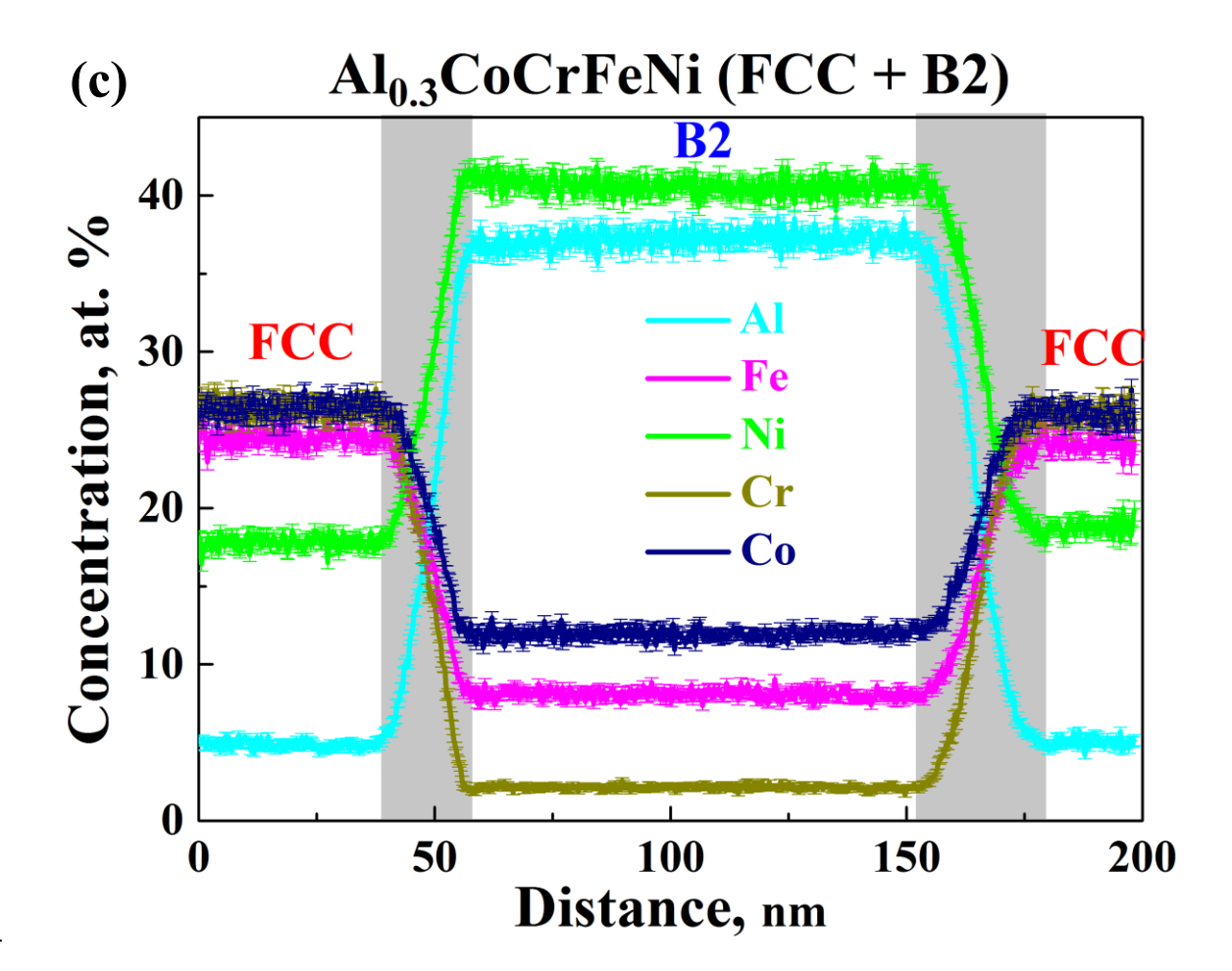
Figure 3 (cont'd)



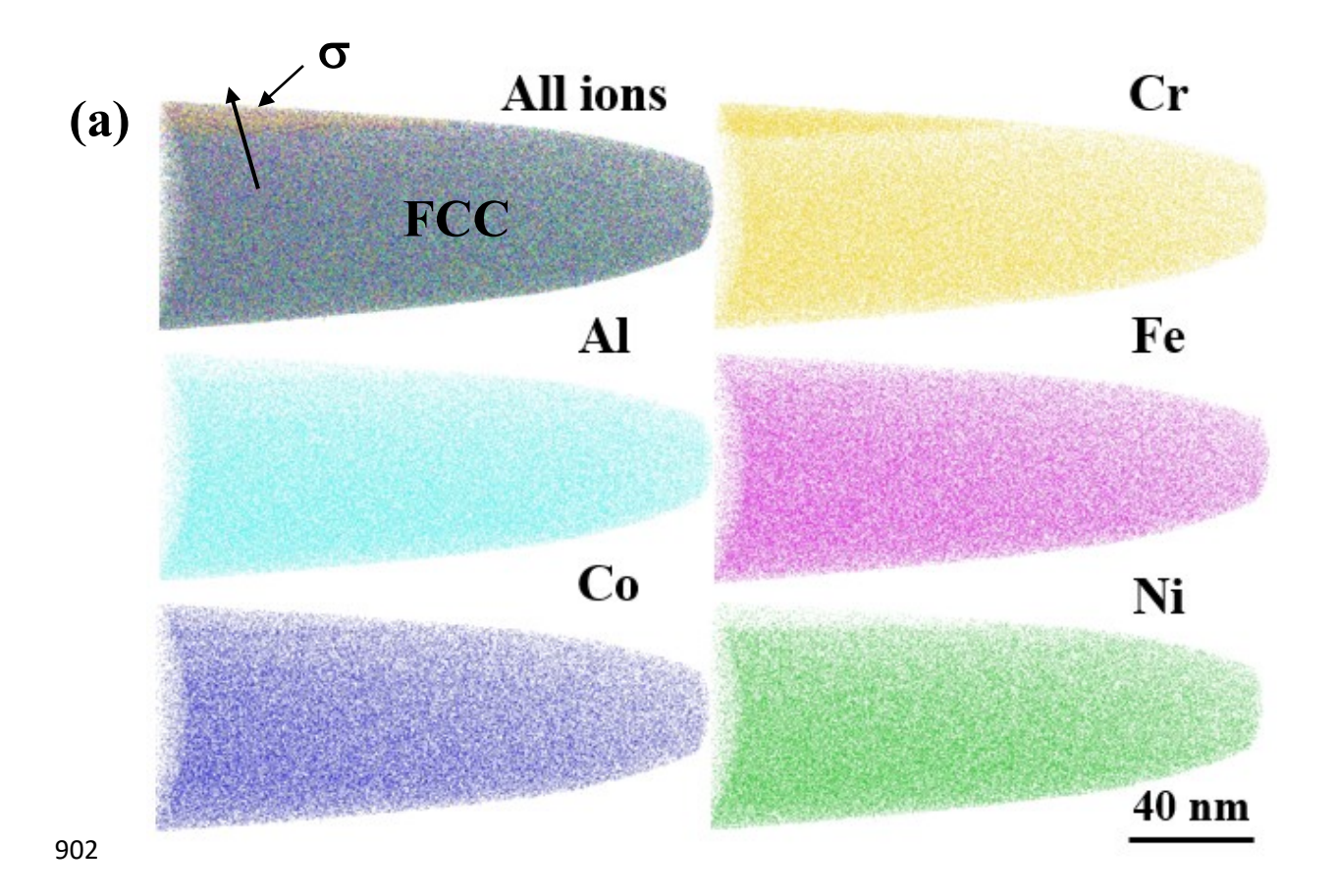
889 Figure 4

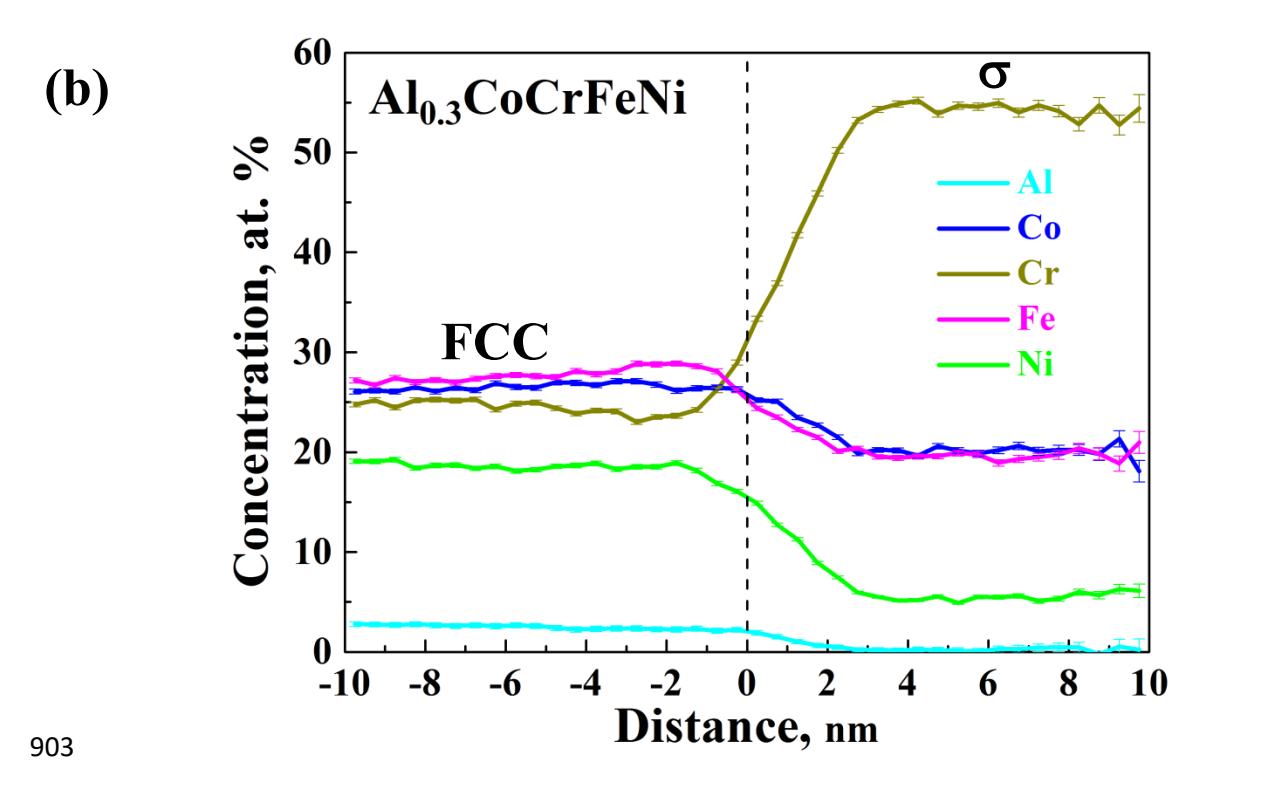
B2

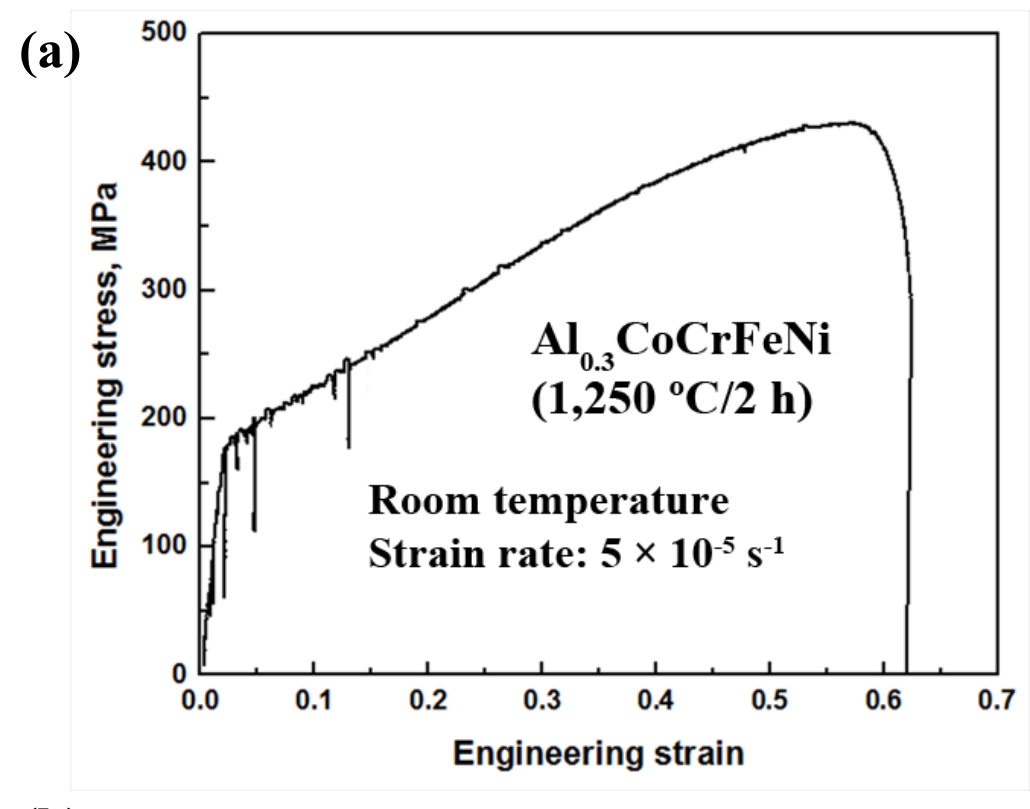
50 nm

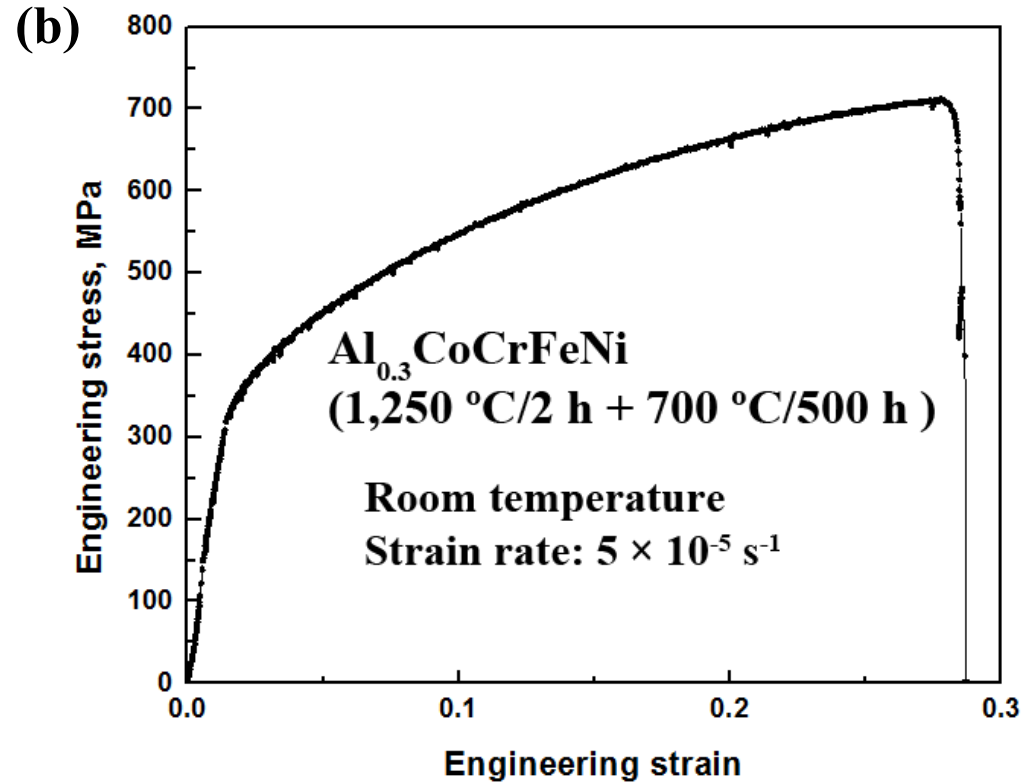


901 Figure 4 (cont'd)

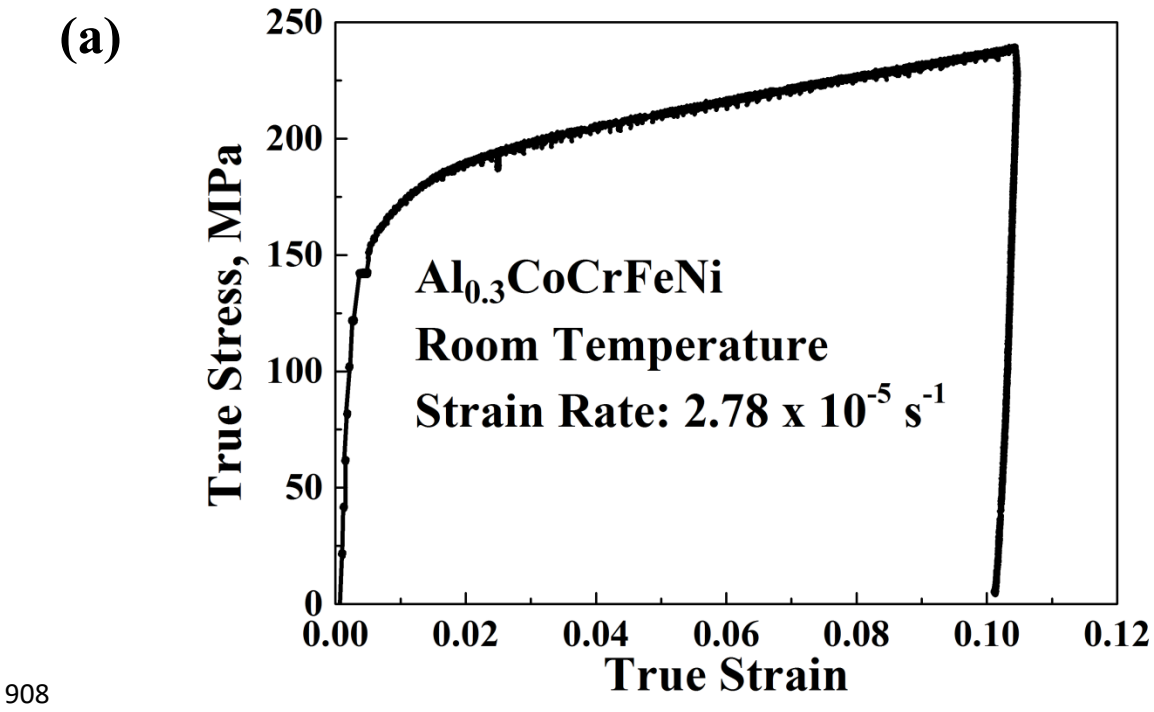


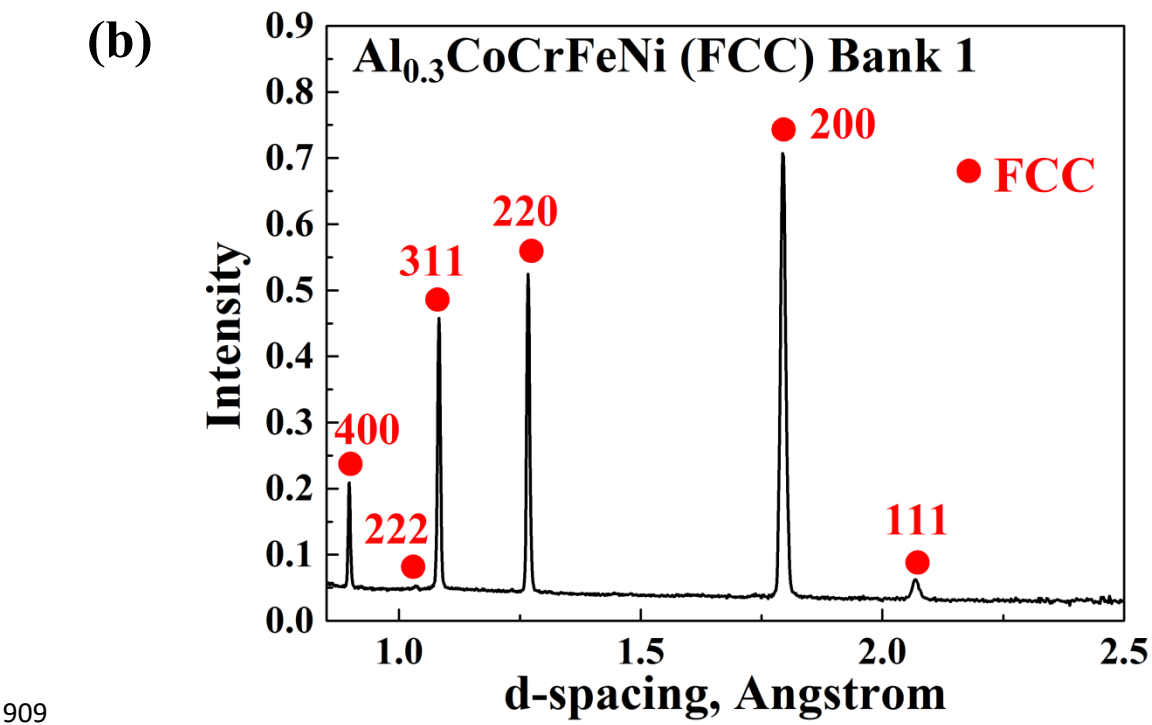


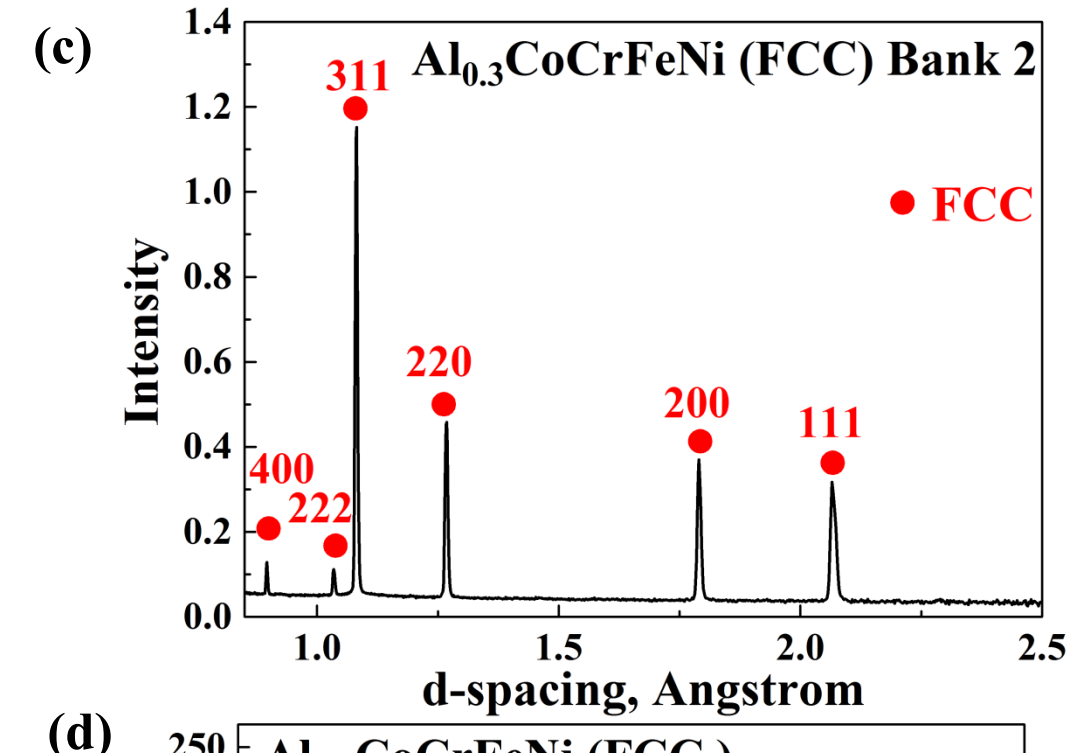




907 Figure 6







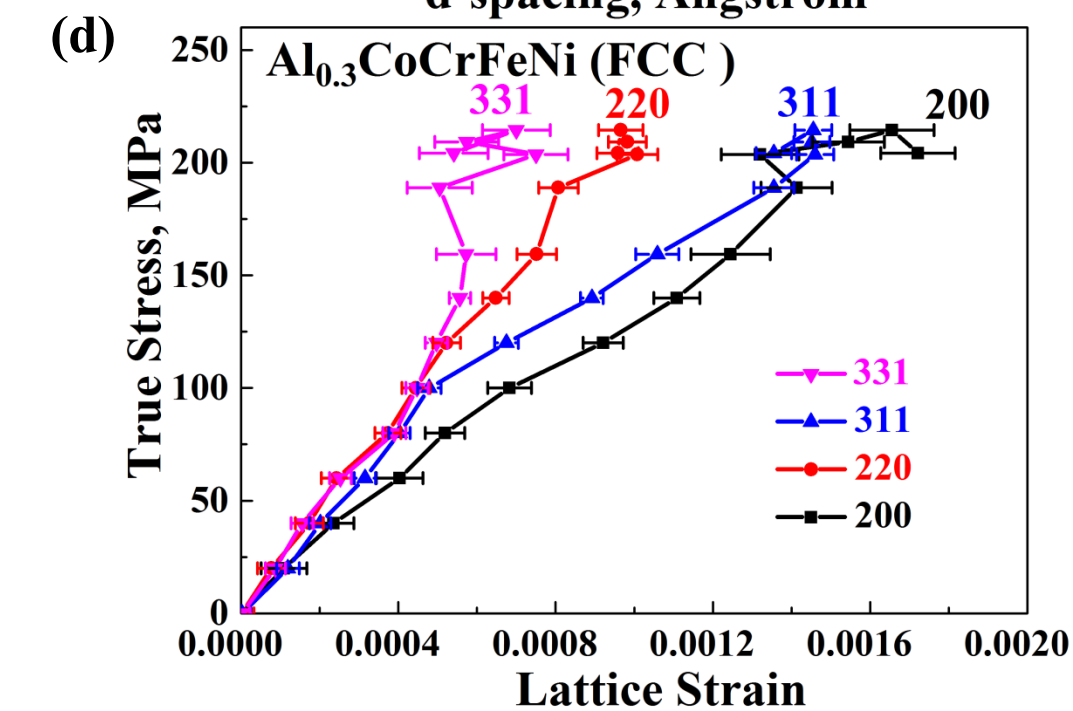
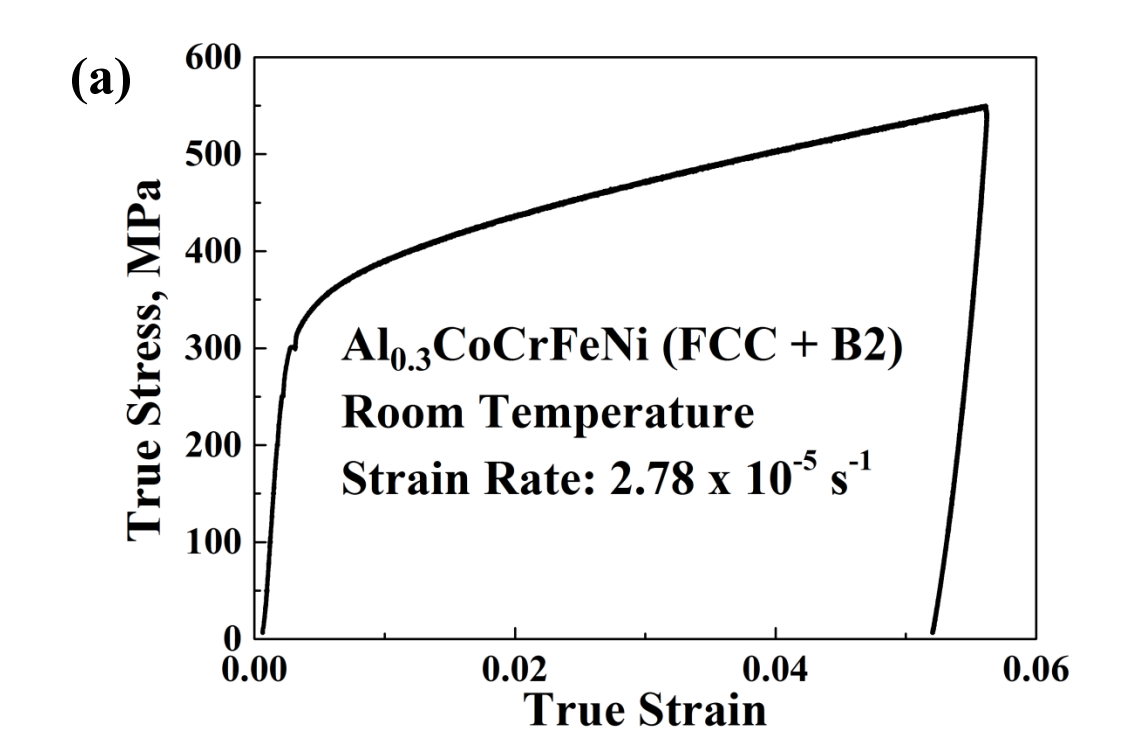
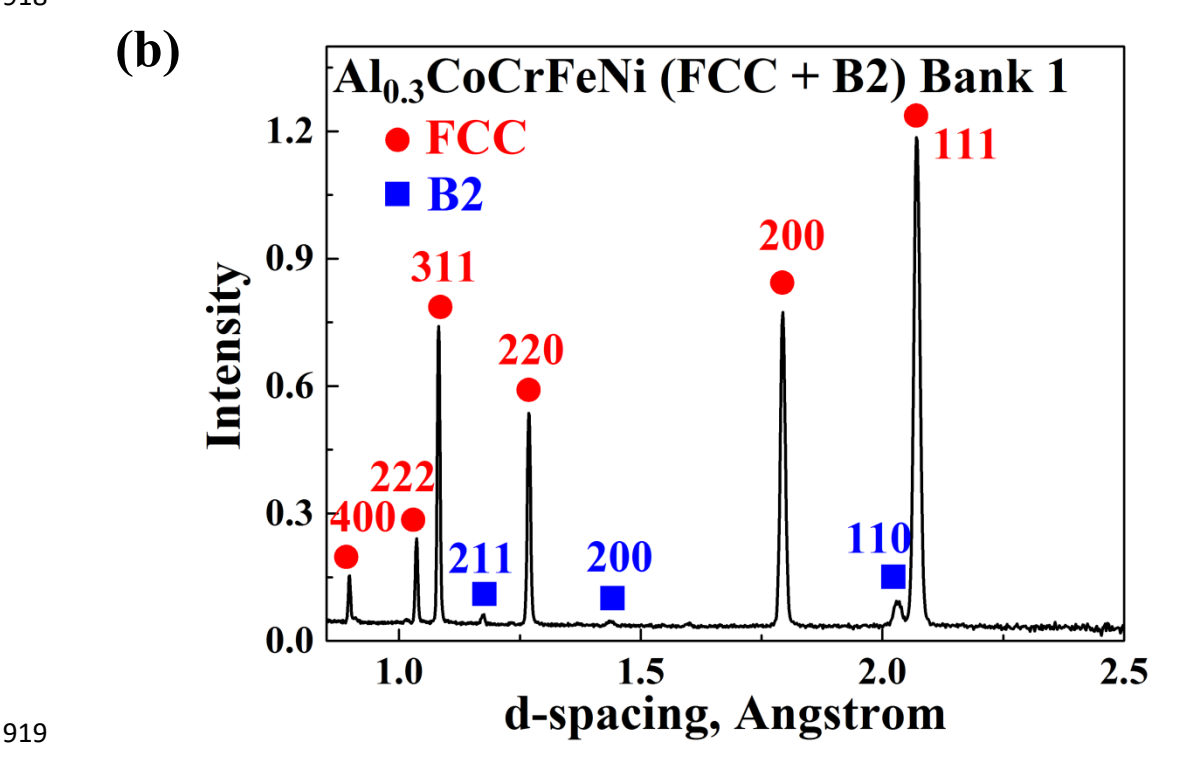
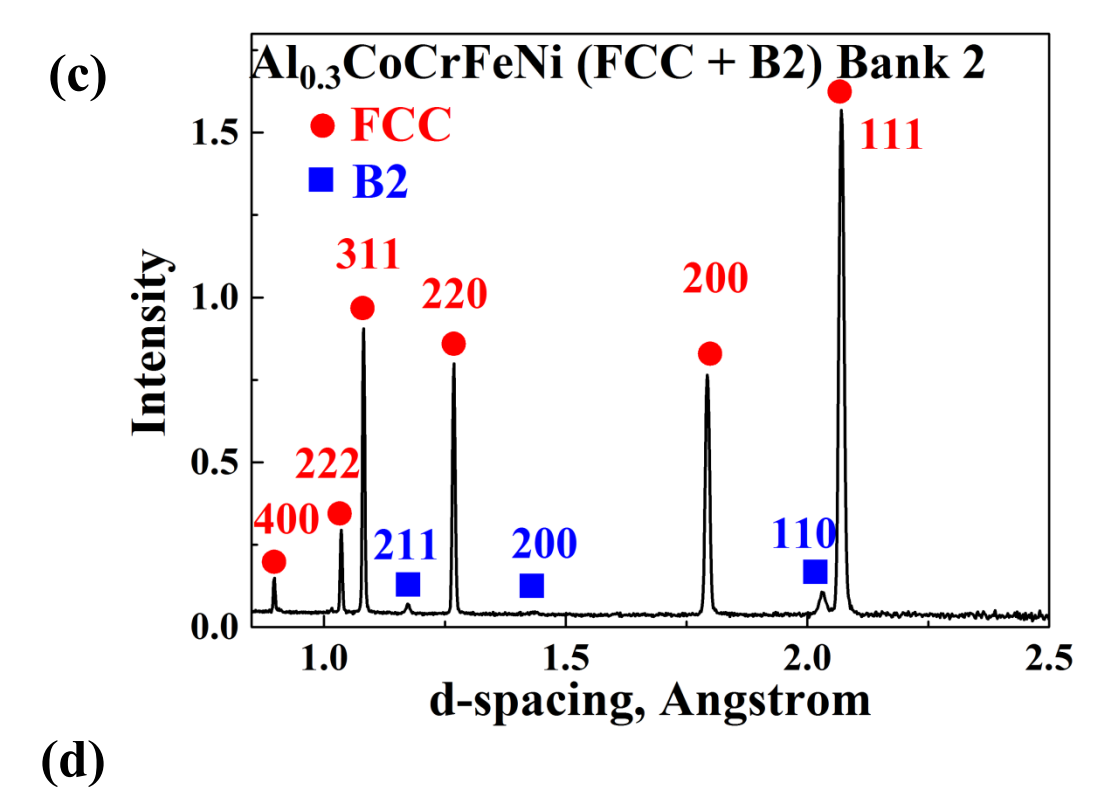


Figure 7 (cont'd)







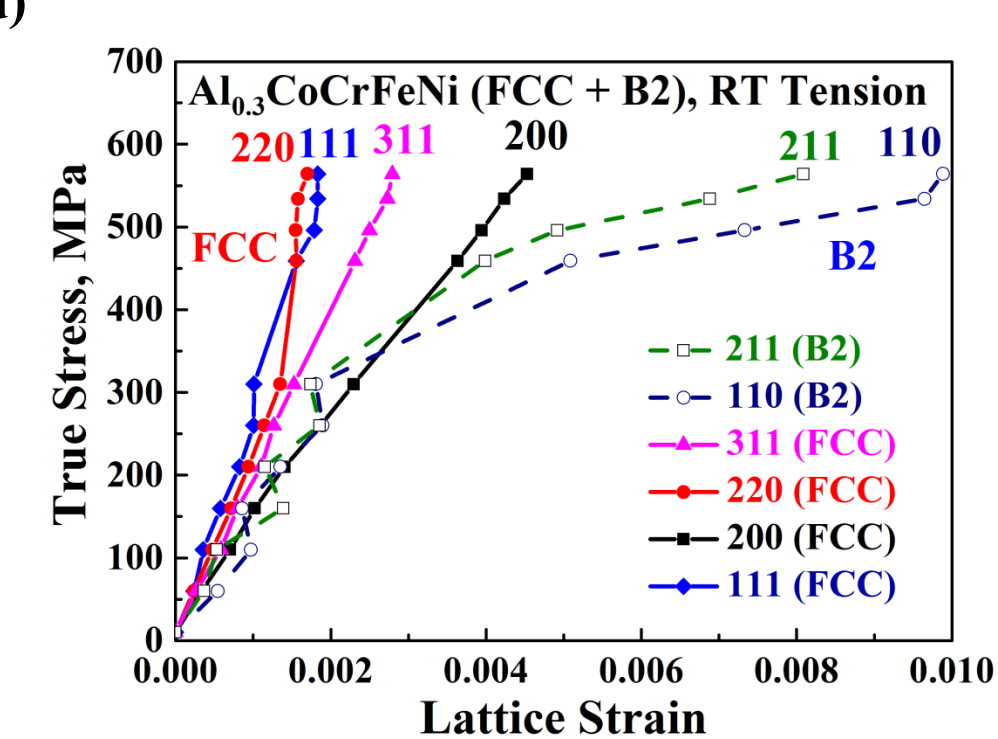
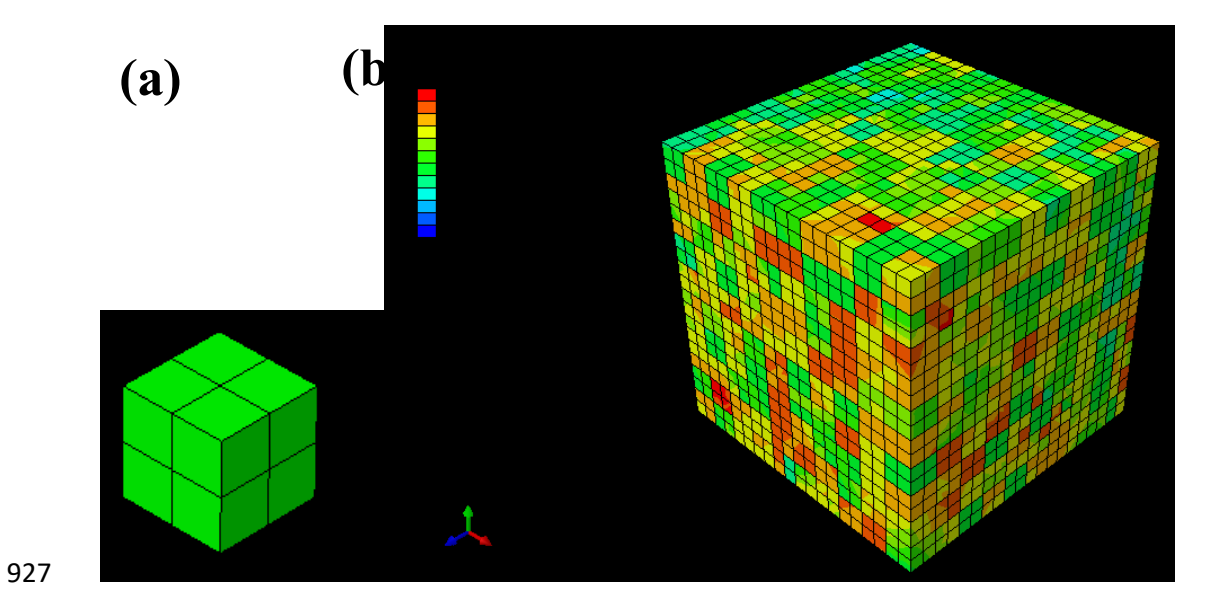
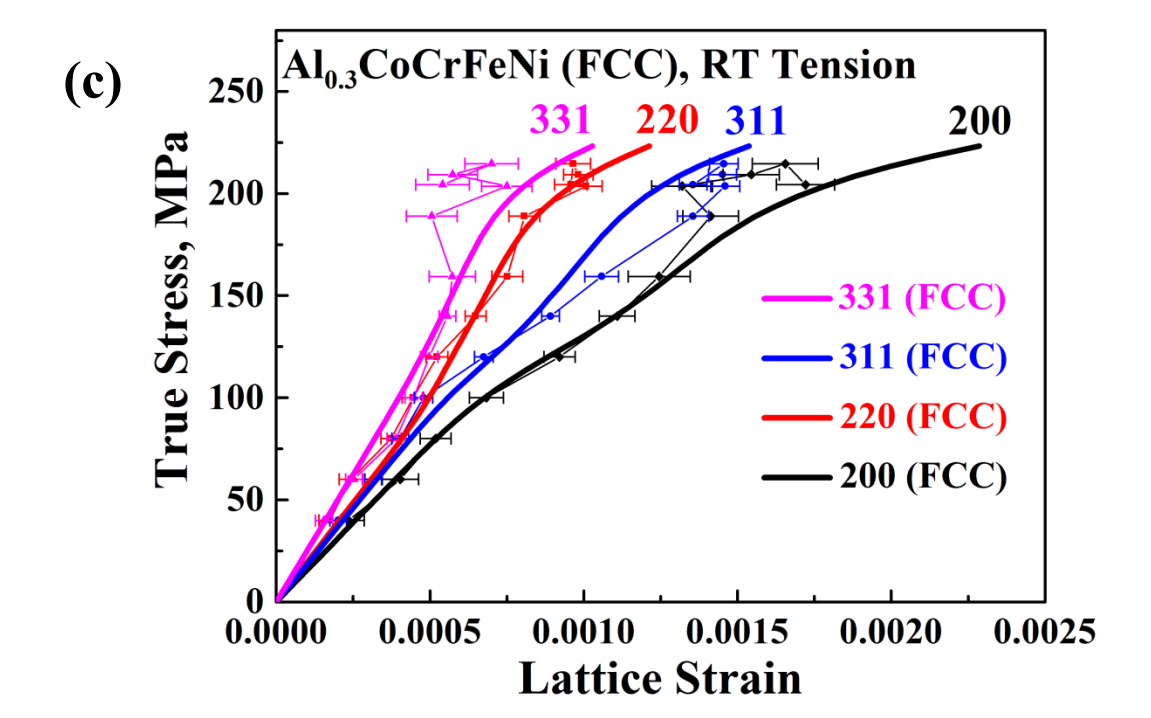
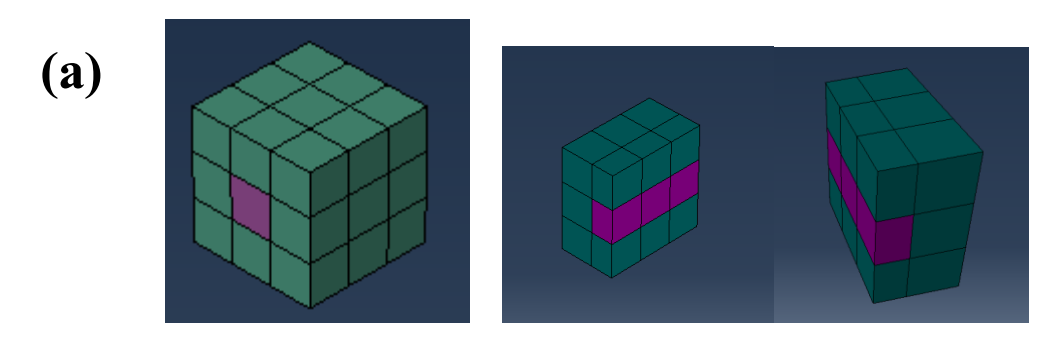


Figure 8 (cont'd)



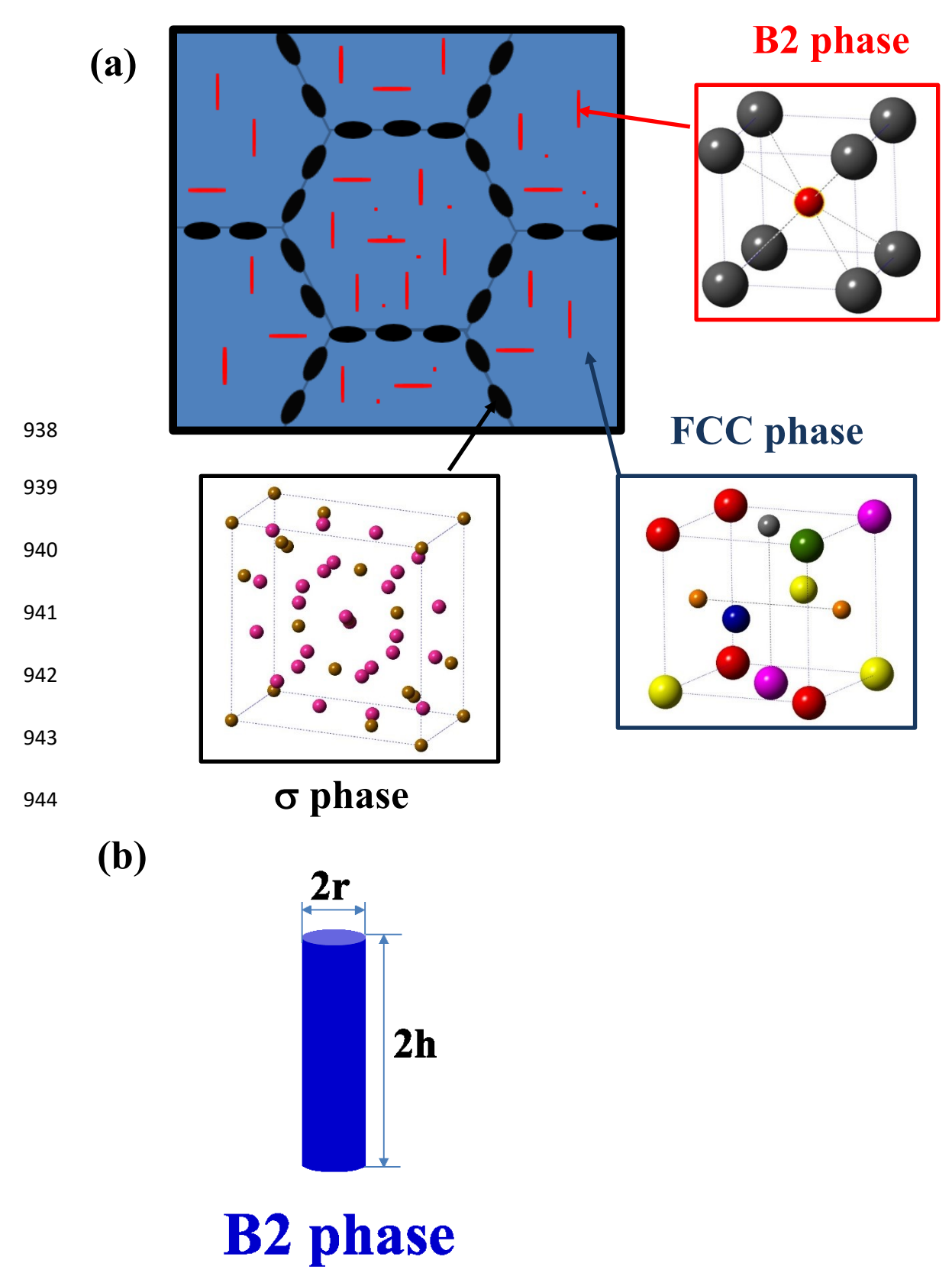


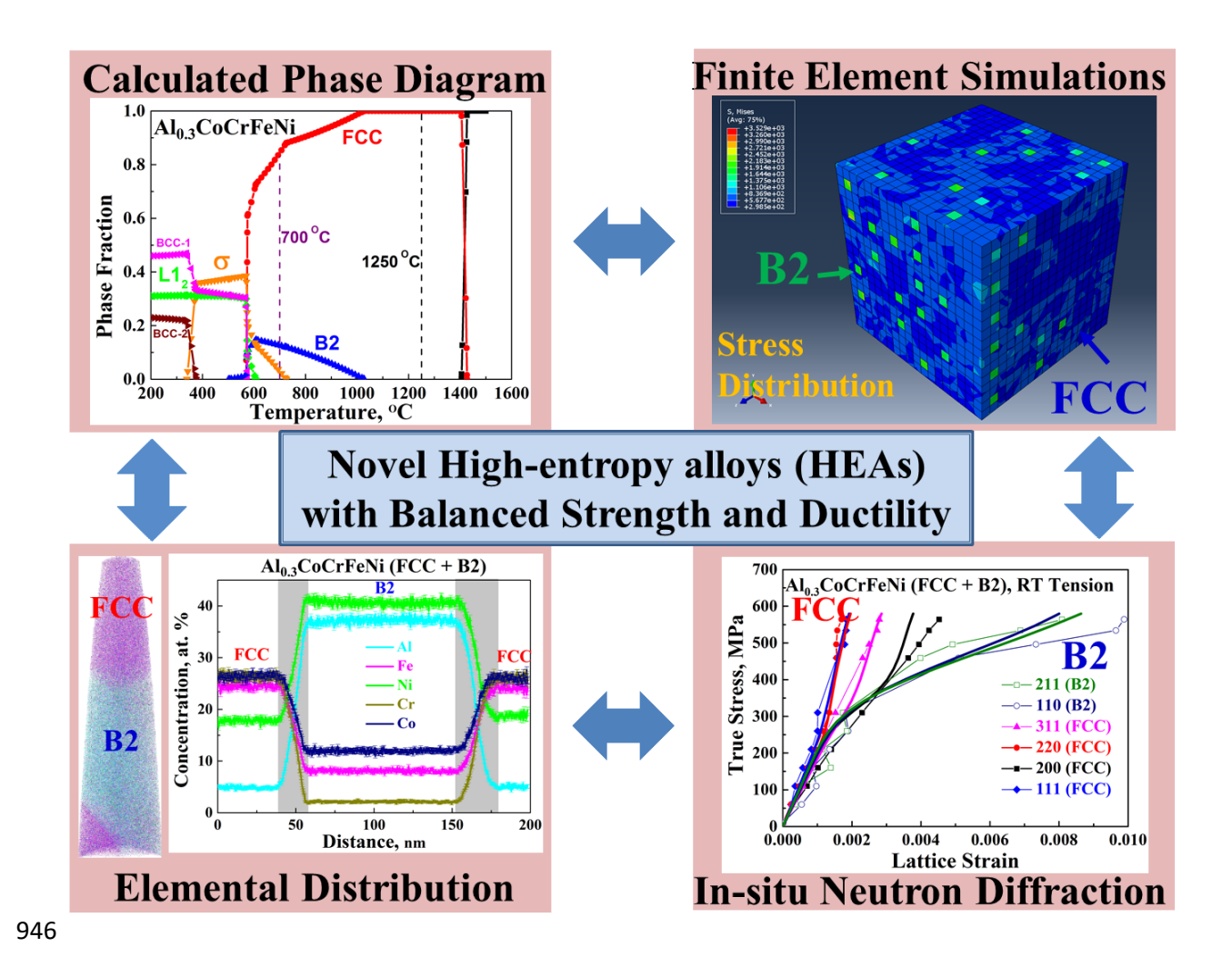


935

936

(c) 700 Al_{0.3}CoCrFeNi (FCC + B2), RT Tension 600 **B2** -211 (B2) -110 (B2) 311 (FCC) - 220 (FCC) - 200 (FCC) 100 **←** 111 (FCC) 0.000 0.002 0.004 0.006 0.008 0.010 **Lattice Strain**





Graphic Abstract